AGU PUBLICATIONS

JGR

Journal of Geophysical Research: Atmospheres

RESEARCH ARTICLE
10.1002/2017JD026472

Key Points:
- WRF-Hydro reproduces observed soil moisture, turbulent fluxes, and land surface temperature at individual sites and as spatial patterns
- Diurnal cycle of latent heat flux varies among ecosystems due to plant transpiration and is affected by the peak timing of precipitation
- Stomatal control on plant transpiration induces mesoscale heterogeneity in the diurnal cycle of the turbulent fluxes within a regional basin

Correspondence to:
E. R. Vivoni,
vivoni@asu.edu

Citation:
Xiang, T., E. R. Vivoni, D. J. Gochis, and G. Mascaro (2017), On the diurnal cycle of surface energy fluxes in the North American monsoon region using the WRF-Hydro modeling system, *J. Geophys. Res. Atmos.*, *122*, 9024–9049, doi:10.1002/2017JD026472.

Received 29 JAN 2017
Accepted 9 AUG 2017
Accepted article online 14 AUG 2017
Published online 4 SEP 2017

On the diurnal cycle of surface energy fluxes in the North American monsoon region using the WRF-Hydro modeling system

Tiantian Xiang[1], Enrique R. Vivoni[1,2], David J. Gochis[3], and Giuseppe Mascaro[1]

[1]School of Sustainable Engineering and the Built Environment, Arizona State University, Tempe, Arizona, USA, [2]School of Earth and Space Exploration, Arizona State University, Tempe, Arizona, USA, [3]National Center for Atmospheric Research, Boulder, Colorado, USA

Abstract The diurnal cycles of surface energy fluxes are important drivers of atmospheric boundary layer development and convective precipitation, particularly in regions with heterogeneous land surface conditions such as those under the influence of the North American monsoon (NAM). Characterization of diurnal surface fluxes and their controls has not been well constrained due to the paucity of observations in the NAM region. In this study, we evaluate the performance of the uncoupled WRF-Hydro modeling system in its ability to represent soil moisture, turbulent heat fluxes, and surface temperature observations and compare these to operational analyses from other commonly used land surface models (LSMs). After a rigorous model evaluation, we quantify how the diurnal cycles of surface energy fluxes vary during the warm season for the major ecosystems in a regional basin. We find that the diurnal cycle of latent heat flux is more sensitive to ecosystem type than sensible heat flux due to the response of plant transpiration to variations in soil water content. Furthermore, the peak timing of precipitation affects the shape and magnitude of the diurnal cycle of plant transpiration in water-stressed ecosystems, inducing mesoscale heterogeneity in land surface conditions between the major ecosystems within the basin. Comparisons to other LSMs indicate that ecosystem differences in the diurnal cycle of turbulent fluxes are underestimated in these products. While this study shows how land surface heterogeneity affects the simulated diurnal cycle of turbulent fluxes, additional coupled modeling efforts are needed to identify the potential impacts of these spatial differences on convective precipitation.

1. Introduction

The North American Monsoon (NAM) system is an important large-scale circulation pattern in the southwest U.S. and northwest Mexico where it supplies between 40 and 85% of the total annual precipitation [e.g., *Douglas et al.*, 1993; *Adams and Comrie*, 1997; *Vivoni et al.*, 2010]. Although regional climate models (RCMs) can reproduce some features of the NAM, its overall seasonal cycle, the magnitude, spatial extent, and evolution of the system are still not predicted accurately [e.g., *Liang et al.*, 2008; *Castro et al.*, 2012; *Stensrud*, 2013]. On shorter time scales, there is also limited predictability in the timing, location, and intensity of diurnal convection, in particular over mountainous terrains [*Gochis et al.*, 2002; *Collier and Zhang*, 2006; *Gao et al.*, 2007]. For example, the strong diurnal cycle of clouds and precipitation observed from ground and remote sensing platforms [*Gochis et al.*, 2007; *Nesbitt et al.*, 2008; *Mascaro et al.*, 2014] are poorly represented in RCMs tailored to study the NAM system [e.g., *Li et al.*, 2004; *Gutzler et al.*, 2005; *Lee et al.*, 2007, 2008; *Yamada et al.*, 2012].

Despite its importance as a driver of convective precipitation [*Betts et al.*, 1996], the diurnal cycle of turbulent fluxes, namely, sensible and latent heat fluxes, has not been examined in the NAM system from observations or RCM simulations [c.f., *Gutzler et al.*, 2009], largely due to the fact that very few observations of such fluxes exist. Diurnal changes in turbulent fluxes over complex terrain have important implications on boundary layer development, mountain-valley circulations, and convection [*Eltahir*, 1998; *Sturman et al.*, 1999; *Whiteman et al.*, 2000; *Feng et al.*, 2013]. Observations of these fluxes in the region have been limited to a small number of sites [e.g., *Vivoni et al.*, 2008a; *Pérez-Ruíz et al.*, 2010; *Pierini et al.*, 2014; *Glenn et al.*, 2015] and have mostly focused on seasonal variations. For example, *Méndez-Barroso et al.* [2014] compared monsoon season latent heat fluxes in two ecosystems organized along a topographic gradient. The authors found that vegetation greening varied with elevation and dictated the timing and magnitude of the seasonal evapotranspiration pulse. Whether or not there is a link between the diurnal cycle of turbulent fluxes occurring

on complex terrain and the strong diurnal variations in convective precipitation [*Gochis et al*., 2007; *Nesbitt et al*., 2008] has yet to be established.

To identify if such a link exists requires a coupled land-atmosphere modeling system that represents diurnal and seasonal variations in land surface processes. The evolution of land surface models (LSMs) from simple representations [e.g., *Manabe*, 1969; *Sellers et al*., 1997] to physically based models with realistic feedbacks [e.g., *Pitman*, 2003] offers the prospect of addressing this question. To simulate hydrologic processes over complex terrain, many efforts have been made to incorporate new physics into LSMs. These include vegetation impacts on canopy interception, evaporation and transpiration [e.g., *Wigmosta et al*., 1994], topographic impacts on soil water drainage and redistribution [e.g., *Choi et al*., 2013; *Beven et al*., 1995], and snow processes [e.g., *Lehning et al*., 2006]. However, as a prerequisite of a coupled land-atmosphere modeling study, the offline performance of a land surface model should be evaluated [*Dirmeyer et al*., 1999; *Mitchell et al*., 2004; *Boone et al*., 2004]. Prior efforts have mainly focused on model comparisons, such as the African Monsoon Multidisciplinary Analysis land surface model intercomparison [*Boone et al*., 2009] that focused on the West African monsoon. Although useful in providing guidance for evaluating land surface models, intercomparison studies typically do not directly engage in process diagnostics. For warm season convective systems over complex terrain, such as those occurring in southwestern North America, a more detailed, process-oriented approach that diagnoses multiple land surface variables is required.

As a way forward in this respect, the WRF-Hydro modeling system integrates multiple land surface representations with the mesoscale Weather Research and Forecast (WRF) model [*Gochis et al*., 2014; *Yucel et al*., 2015; *Senatore et al*., 2015]. A series of enhancements have been made in WRF-Hydro that attempt to improve the simulation of terrestrial hydrologic processes at high spatial and temporal resolutions, including lateral redistribution of overland and saturated subsurface flows for runoff prediction. The multiparameterization Noah (Noah-MP) [*Niu et al*., 2011] land surface model is available as a column LSM option in WRF-Hydro, which provides a suite of canopy and surface energy exchange processes to account for the exchanges of water and energy between the atmosphere and multiple-layer soil columns. Specifically, several time-varying vegetation options in Noah-MP allow the use of prescribed or dynamic parameters such as vegetation fraction (VF) and leaf area index (LAI). When combined with the high-resolution routing grid of WRF-Hydro, capable of redistributing soil moisture and updating information to the Noah-MP coarse LSM grid, we hypothesize that these enhancements should improve the model's ability to capture seasonal and finer time scale variations of land surface properties during the NAM, which, in turn, are expected to significantly influence the surface energy partitioning at the subdaily time scale [e.g., *Vivoni*, 2012; *Kumar et al*., 2014].

In this study, we evaluate the performance of the Noah-MP model embedded within the WRF-Hydro modeling system for representing the diurnal cycle of surface energy fluxes during the NAM. The study is organized in a progression that begins with evaluations at two different scales using a range of available observations to build model confidence, followed by analyses of the diurnal cycle of surface energy fluxes for cases where lateral water movements are simulated and a comparison to land surface models where these physical processes are captured a coarser resolution. Model evaluation activities are first carried out in reference to ground-based observations of soil moisture and turbulent fluxes using one-dimensional (1-D) simulations at measurement sites in the study area. Then, using the calibrated soil parameters from the 1-D cases, spatially distributed simulations are conducted in a large river basin in the NAM region to capture the spatial patterns of soil properties, terrain attributes, and seasonally varying vegetation. Simulations from two monsoon seasons (2004 and 2013) are then compared against remotely sensed estimates of land surface temperature, evapotranspiration, and surface soil moisture. After assessing the fidelity of the WRF-Hydro simulations, we then explore the diurnal cycle of surface energy fluxes across a range of different ecosystems. Lastly, we compare the results to a set of coarser resolution, operational off-line land surface models. To our knowledge, this is the first study attempting to characterize the fine-scale spatial and temporal variabilities of the diurnal cycle of surface energy fluxes during the monsoon season through combined use of available observations and a high-resolution modeling system such as WRF-Hydro.

2. Methods

2.1. Study Region and Its Characteristics

The study region is the Rio Sonora Basin (RSB; 21,264 km^2 in area) located in northern Sonora, Mexico (Figure 1a). As part of the Sierra Madre Occidental, a major physiographic region of North America, the

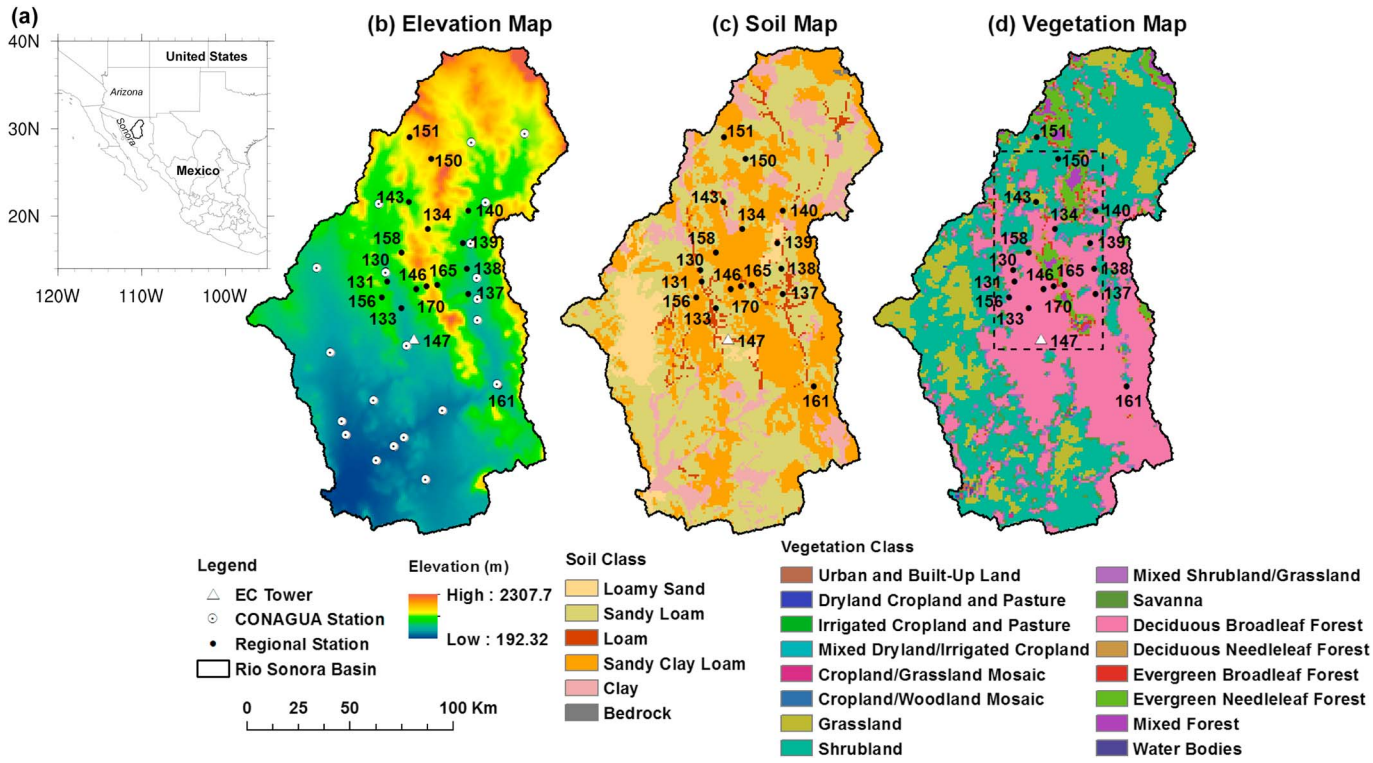

Figure 1. (a) Location of the Rio Sonora Basin in Sonora, Mexico. (b) Elevation distribution obtained at 90 m resolution from *Lehner et al*. [2008] and regridded to 100 m resolution for use in WRF-Hydro. (c) Soil texture classification from *INEGI* [2007] at 650 m resolution and regridded to 1 km. (d) Land cover classification from *Loveland et al*. [2000] at 1 km resolution. The location of 18 regional hydrometeorological stations and one eddy covariance (EC) tower are depicted. The rectangular box in Figure 1d represents the extent of the 2D-STAR soil moisture data.

north-south oriented watershed is composed of elevations ranging from 192 m to 2308 m (Figure 1b) at 90 m resolution, as obtained from *Lehner et al*. [2008] and regridded to 100 m resolution for use in Noah-MP and WRF-Hydro. Geological processes that gave rise to the mountain and valley systems within the RSB also produce a complex arrangement of soil properties. Figure 1c depicts the surface soil texture classification from the Instituto Nacional de Estadística y Geografía [*INEGI*, 2007] at 620 m resolution and regridded to 1 km resolution, with the dominant soil classes as sandy loam and sandy clay loam, followed by clay and loamy sand. The RSB has an arid to semiarid climate (Koppen-Geiger classification varying from hot desert, BWh, to steppe or semiarid, BSh), with mean annual precipitation from 350 mm to 700 mm [*Hallack-Alegría and Watkins*, 2007], of which 40 to 70% falls during the summer monsoon from July to September [*Vivoni et al*., 2008a; *Robles-Morua et al*., 2015]. Spatial variations in climatic conditions resulting from latitudinal and elevation gradients [*Mascaro et al*., 2015] have led to a wide range of ecosystems (Figure 1d), including shrublands, grasslands, deciduous broadleaf forests, evergreen needleleaf, and evergreen broadleaf forests, as captured at 1 km resolution in the land cover classification of *Loveland et al*. [2000]. Regional vegetation greening during the monsoon varies depending on the plant functional type and the ecosystem arrangements along latitudinal and elevation gradients [e.g., *Forzieri et al*., 2011, 2014].

2.2. Ground Observations and Remote Sensing Products

A network of ground observations was established in the RSB as part of the North American Monsoon Experiment-Soil Moisture Experiment in 2004 (NAME-SMEX04) [*Higgins and Gochis*, 2007] and subsequently expanded upon. Figure 1 depicts the locations of the regional hydrometeorological network, including 18 stations measuring hourly precipitation (*P*) using a tipping-bucket rain gauge (Texas Electronics, TR525I), and soil moisture (SM) at 5 cm depth using a soil dielectric sensor (Stevens Hydra Probe). *Vivoni et al*. [2007] discuss measurement techniques and the local calibrations performed. In addition, an eddy covariance (EC) tower was installed with a full suite of meteorological variables and turbulent flux measurements, including sensible heat flux (*H*) and evapotranspiration (ET), as detailed in *Méndez-Barroso et al*. [2014]. During a

Table 1. Locations (Latitude, Longitude, and Elevation) and Characteristics (Vegetation and Soil Classes) of the Regional Hydrometeorological Stations, Including the Calibration and Validation Years Used in the 1-D Noah-MP Simulations (Summer Precipitation From May to September Reported in Parentheses)[a]

Station ID	Lat. (deg)	Lon. (deg)	Elev. (m)	Veg. Class	Soil Class	Cal. Year (*P* in mm)	Val. Year (*P* in mm)
130	30.04	−110.67	724	DBF	SL	2004 (217)	2013 (287)
131	29.99	−110.67	741	DBF	SL	-	2013 (356)
132	29.96	−110.52	905	DBF	SCL	2004 (249)	2013 (355)
143	30.34	−110.56	960	GR	L	2004 (170)	-
146	29.97	−110.47	1375	DBF	SCL	2004 (315)	2013 (395)
147*	29.74	−110.54	724	DBF	LS	2004 (278)	-
134	30.22	−110.46	1180	DBF	SCL	-	2004 (271)
137	29.94	−110.26	660	DBF	SL	-	2004 (300)
138	30.05	−110.27	722	DBF	SL	-	2004 (293)
139	30.16	−110.29	758	DBF	LS	-	2004 (292)
140	30.30	−110.26	1017	SH	SCL	-	2004 (331)
150	30.53	−110.44	1506	SH	SL	-	2013 (391)
151	30.62	−110.55	1412	SH	SCL	-	2013 (350)
156	29.92	−110.69	929	SA	SCL	-	2013 (356)
158	30.12	−110.60	1203	SA	SCL	-	2013 (463)
161	29.53	−110.11	499	DBF	SCL	-	2013 (411)
165	29.98	−110.42	858	DBF	SCL	-	2013 (395)
170	29.96	−110.46	1334	DNF	SCL	-	2013 (395)

[a]Vegetation classes and their areal percent in RSB are shrubland (SH, 38.16%), deciduous broadleaf forest (DBF, 32.62%), grassland (GR, 12.22%), savanna (SA, 4.16%), and deciduous needleleaf forest (DNF, 4.13%). Soil classes and their areal percent are sandy loam (SL, 44.67%), sandy clay loam (SCL, 34.30%), loamy sand (LS, 6.32%), and loam (L, 2.80%). EC tower is labeled with an asterisk. The hyphens indicate the stations that were not used.

field campaign in 2013, the hydrometerological observation network was operated. Table 1 describes the locations of the regional stations and the EC tower, including their vegetation and soil classes as determined from the geospatial data used within WRF-Hydro, which generally agree with site-specific information. The stations span a wide range of geographic locations (Figure 1) and elevations (from ~500 to 1500 m) and represent nearly 90% of the RSB area in terms of the vegetation and soil characteristics. Precipitation and soil moisture data from the regional stations and the full suite of meteorological variables and fluxes at the EC towers were subject to various levels of processing and quality-control procedures discussed in *Vivoni et al*. [2007, 2008b], *Méndez-Barroso et al*. [2014], and *Mascaro et al*. [2015]. To supplement the sparse areal coverage of the ground-based precipitation data in the study region, we also utilized the daily precipitation records from the Comisión Nacional del Agua (CONAGUA) at 21 sites located within the RSB (see Table 2 for a description). These stations span a wide elevation range (298 to 1056 m), with a mean of 530 m and a standard deviation of 230 m (Figure 1b).

To characterize land surface conditions, we relied on the Moderate Resolution Imaging Spectroradiometer (MODIS) sensor and the 2-D Synthetic Aperture Radiometer (2D-STAR) [*Ryu et al*., 2010; *Mascaro and Vivoni*, 2012] airborne product. Details of the remote sensing products are described in Table 2. The spatiotemporal variations of vegetation parameters were obtained from MODIS composites following the methods of *Xiang et al*. [2014] that relate the observed fields directly to Noah-MP vegetation parameters. The remote sensing products were 16 day composites of normalized difference vegetation index (NDVI, MOD13Q1, 250 m spatial resolution) and 8 day composites of LAI (MOD15A2, 1 km). NDVI and LAI have been shown to represent vegetation conditions well in semiarid regions relative to ground data [*Privette et al*., 2002; *Fensholt et al*., 2004; *Ryu et al*., 2012]. Cloud-free MODIS composites were linearly interpolated to daily values to allow gradual vegetation changes. Daily MODIS land surface temperature (LST, MOD11A1, and MYD11A1, 1 km [*Wan and Dozier*, 1996]) and 8 day total evapotranspiration (MOD16, 1 km [*Mu et al*., 2011]) were used for model evaluations, as well as aircraft-based soil moisture retrievals from 2D-STAR. *Xiang et al*. [2014] describe the processing steps undertaken for the LST products (MOD11A1). Figure 2 presents the time series of basin-averaged variables extracted from remotely sensed data over the period 2004–2014. Note the seasonal and interannual variations in vegetation conditions, as depicted by VF and LAI representing the horizontal and vertical structures of vegetation, as well as the seasonal variations in LST. Based on the availability of ground and remote sensing data, we selected the summers of 2004 and 2013 to conduct distributed simulations in the

Table 2. Data Set Characteristics Classified as Model Output (MO), Remote Sensing Data (RS), or Ground Observations (GO)[a]

Source	Type	Variables	Spatial/Temporal Resolution	Usage
NLDAS-2	MO	P, P_s, IS, RH, T_a, w	12 km, 1 h	Meteorological forcings
CONAGUA	GO	P	Point, daily	NLDAS correction
ASU-UNISON	GO	P	Point, hourly	NLDAS correction
		SM, LST		Model calibration and validation
MODIS	RS	NDVI	250 m, 16 day composite	Derivation of vegetation parameters
		LAI	1000 m, 8 day composite	
		LST	1000 m, daily	Model validation
		ET	1000 m, 8 day total	
2D-STAR	RS	SM	800 m, snapshot	Model validation

[a]The variables are precipitation (P), atmospheric pressure (P_s), incoming solar radiation (IS), relative humidity (RH), air temperature (T_a), wind speed (w), soil moisture (SM), land surface temperature (LST), normalized difference vegetation index (NDVI), leaf area index (LAI), and evapotranspiration (ET).

RSB (1 May to 30 September), whereas 1-D simulation at individual stations spanned different calibration and validation periods (Table 1). As shown in Figure 2, the two study periods contain vegetation greening with similar peak values of VF and LAI, which makes them suitable for analysis of land surface conditions under comparable vegetation states. Additional attention was placed on the 2004 season due to the observational and process studies conducted during NAME-SMEX04.

2.3. Meteorological Forcing Products

Hourly meteorological forcings for the distributed simulations were obtained from the North American Land Data Assimilation System (NLDAS-2) [*Mitchell et al*., 2004; *Xia et al*., 2012] at a resolution of 1/8th degree (~12 km). The consistent set of high-resolution variables from NLDAS (1979–present) in northern Mexico (>25°N) is a useful alternative for regional applications, in particular when interpolation of sparse station observations is not feasible. Nevertheless, NLDAS forcings have been found to underestimate precipitation in mountainous areas [*Pan et al*., 2003; *Robles-Morua et al*., 2012], a problem exacerbated in northern Mexico, where satellite-derived precipitation estimates are not corrected sufficiently well with ground observations. This underestimation can reach up to 250 mm/yr over high elevation sites in northern Mexico [*Robles-Morua et al*., 2012]. Thus, we applied a daily bias correction following *Robles-Morua et al*. [2012] using precipitation data from the CONAGUA and the Arizona State University and Universidad de Sonora (ASU-UNISON) networks (Table 2). Depending on data availability, the number of stations used in the bias correction varied, with a mean number of 10 stations per day. Bias correction increased summer precipitation (1 May to 30 September) in the RSB from 245 to 298 mm in 2004 and from 288 mm to 383 mm in 2013. Bias-corrected NLDAS rainfall provides the model the best possible spatial forcing that is consistent with

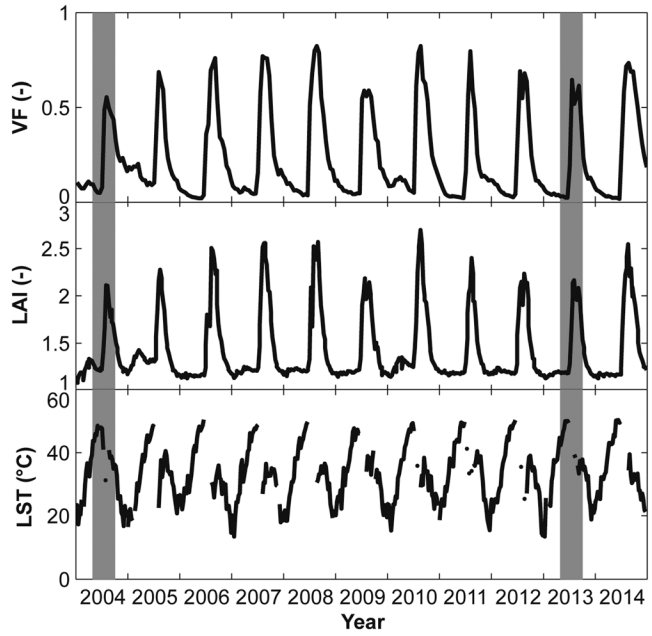

Figure 2. Remotely sensed, basin-averaged vegetation fraction (VF), leaf area index (LAI), and land surface temperature (LST) obtained at 10:30 A.M. from 2004 to 2014. The shaded areas contain the two simulation periods in summer 2004 and 2013. Gaps in LST are due to retrieval errors.

Table 3. Summary of Physics Options in Noah-MP

Physical Processes	Option	References
Canopy stomatal resistance	Ball-Berry scheme	*Ball et al.* [1987], *Sellers et al.* [1997], and *Niu et al.* [2011]
Soil moisture factor for stomatal resistance, β factor	Noah type using soil moisture	*Niu et al.* [2011]
Runoff and groundwater	Infiltration-excess-based surface runoff scheme with gravitational free-drainage subsurface runoff scheme	*Schaake et al.* [1996]
Surface layer drag coefficient	Monin-Obukhov scheme	*Brutsaert* [1982]
Frozen soil permeability	Defined by soil moisture	*Niu and Yang* [2006]
Supercooled liquid water in frozen soil	Generalized freezing-point depression	*Niu and Yang* [2006]
Two-stream radiation transfer	Gaps from vegetated fraction	*Niu and Yang* [2004]
Snow surface albedo	BATS scheme	*Yang et al.* [1997]
Partitioning precipitation into rainfall and snow	Complex functional form	*Jordan* [1991]

ground observations, when alternatives such as weather radar are not available. In addition, we made linear adjustments to atmospheric pressure, air temperature, and wind speed in the NLDAS fields based upon the ground data obtained at the EC tower (station 147) for both summers (1 May to 30 September). Based on a daily comparison, single linear multipliers of 0.998 and 0.995 are applied to the atmospheric pressure and air temperature in the NDLAS forcing. To adjust the 10 m height wind speed obtained from NLDAS forcing to the 2 m height assumed for model input, a linear regression is constructed relating wind speed from NLDAS and the 2 m EC tower observation with a linear multiplier of 0.455. When conducting 1-D simulations at the regional stations and EC tower, we compared the model outputs obtained using rain gauge data and the bias-corrected NLDAS pixel values to quantify the biases introduced by utilizing the meteorological forcing products developed for the RSB.

2.4. WRF-Hydro Modeling System Description

The WRF-Hydro modeling system was set up using multiple grid structures in the RSB such that the Noah-MP land surface scheme operated at 1 km resolution with a representation of overland and channel routing on a nested 100 m grid [e.g., *Gochis and Chen*, 2003; *Gochis et al*., 2014]. The Noah-MP LSM adopts a four-layer soil model (10, 30, 60, and 100 cm thickness) for soil infiltration and redistribution. When the routing option is turned on, a fine resolution grid (100 m) with capability of resolving local topography will further redistribute terrestrial moisture. Subsequently, surface water head and soil moisture content for each soil layer will be aggregated and updated in the coarse Noah-MP LSM grid. Through our modeling experiments, we found that WRF-Hydro can effectively redistribute soil moisture and affect surface energy partitioning, especially over riparian zones, as compared to Noah-MP. However, its overall effect in arid to semiarid regions is not as large as anticipated in more humid regions. Penman potential evaporation is used to estimate evaporation from canopy interception, soil surfaces, and plant transpiration [*Mahrt and Pan*, 1984; *Pan and Mahrt*, 1987]. Physics options adopted in the study are summarized in Table 3. To simulate surface energy fluxes over different land cover types, Noah-MP separates the canopy layer from bare and vegetated ground surfaces, allowing an explicit computation of energy and water exchanges for each component. Over a grid cell, the net solar radiation absorbed by canopy and ground surfaces is partitioned into upward longwave radiation (L_a) and latent (λE), sensible (H), and ground (G) heat fluxes, with each term applied over a vegetated fraction (VF), consisting of canopy and vegetated ground and the bare soil (1-VF) fraction. In addition, the time variation of vegetation properties can be accounted for in a number of ways [*Rosero et al*., 2010]. In this study, we used a vegetation option that allows for a time-varying VF obtained from MODIS NDVI as well as a monthly LAI for various vegetation types based on MODIS (Figure 2). The rooting depth associated with a vegetation class is kept static to match the constant deep rooting profiles of water-limited ecosystems [*Collins and Bras*, 2007]. Preliminary tests in five different ecosystems revealed that the 1-D simulations were sensitive to the temporal variation of VF and LAI. Prescribing static vegetation parameters with the minimal or maximum values during the 2004 monsoon season resulted in changes in total ET ranging from −33.8% to 17%, as compared to the simulation with the time-varying vegetation parameters. These outcomes suggested the importance of capturing the seasonal evolution of vegetation conditions in the model simulations, consistent with prior efforts by *Vivoni* [2012].

Table 4. Soil Parameters Used in 1-D Noah-MP and Distributed WRF-Hydro Simulations

Parameter	Variable (Unit)	Loamy Sand (LS)	Sandy Loam (SL)	Loam (L)	Sandy Clay Loam (SCL)	Clay (C)	Bedrock (B)
Percentage of basin area	A (%)	6.32	44.67	2.80	34.30	11.77	0.14
B parameter[a]	BB (−)	2.00	0.80	7.00	2.00	11.55	2.79
Dry soil moisture threshold[b]	DRYSMC (m^3/m^3)	0.028	0.047	0.066	0.067	0.138	0.006
Soil thermal diffusivity/ conductivity coefficient[b]	F11 (m)	−1.044	−0.569	−0.327	−1.491	−2.138	−1.111
Porosity[b]	MAXSMC (m^3/m^3)	0.421	0.434	0.439	0.404	0.468	0.200
Field capacity[b]	REFSMC (m^3/m^3)	0.383	0.383	0.329	0.314	0.412	0.170
Saturation soil matric potential[b]	SATPSI (m)	0.036	0.141	0.355	0.135	0.468	0.069
Saturation soil conductivity[b]	SATDK (m/s)	1.41×10^{-5}	5.23×10^{-6}	3.38×10^{-6}	4.45×10^{-6}	9.74×10^{-7}	1.41×10^{-4}
Saturation soil diffusivity[b]	SATDW (m^2/s)	5.14×10^{-6}	8.05×10^{-6}	1.43×10^{-5}	9.90×10^{-6}	1.12×10^{-5}	1.36×10^{-4}
Wilting point soil moisture[b]	WLTSMC (m^3/m^3)	0.028	0.047	0.066	0.067	0.138	0.006
Soil quartz content[b]	QTZ (%)	0.82	0.60	0.40	0.60	0.25	0.07

[a]Model calibration.
[b]Default soil parameters.

2.5. Model Evaluation With Observations

We conducted simulations for 1-D configurations at regional stations and EC tower and for distributed domains with interacting grids in the RSB. We labeled the cases at individual sites as 1-D "Noah-MP" simulations and the cases over the entire basin as distributed "WRF-Hydro" simulations. In all cases, the initial soil moisture on 1 May was set as 0.02 m^3/m^3, which is close to the residual soil moisture parameter value, given the prolonged dry conditions prior to the monsoon season, as in *Xiang et al*. [2014] and *Méndez-Barroso et al*. [2014]. As a result, no additional model spin-up was included in the seasonal simulations, though some analyses were restricted from July to September to focus on the NAM. As shown in Table 1, model calibration and validation were performed at 18 stations by using the bias-corrected weather variables from the corresponding NLDAS pixel and precipitation data from each station. Time-varying VF and LAI from the overlying MODIS pixel were also used to parameterize the 1-D simulations. Model calibration focused on varying soil parameters within physically reasonable ranges to minimize the root-mean-square error (RMSE) between observed and simulated SM at five regional stations. Stations represented the four major soil types of the RSB found in 88% of basin area (sandy loam, sandy clay loam, loam, and loamy sand). For two additional classes representing 12% of the basin (clay and bedrock), soil parameters were obtained from the default values in the Noah-MP soil parameter table. Table 4 presents parameter values for each soil class. The only calibrated soil parameter was the pore size distribution index (*B* parameter), while the others are kept as the model default values. Calibrated soil parameters in specific classes were then transferred to stations utilized for model validation and to the distributed simulations in the RSB during 2004 and 2013. As a result, the distributed simulations based on the bias-corrected NLDAS forcing, including precipitation, can also serve as a means to validate the default model performance. Differences in model outputs between the 1-D and distributed simulations at the regional stations might be due either to variations in precipitation (ground observation or bias-corrected NLDAS) or the effects of lateral surface and subsurface routing on the local hydrologic dynamics. Additional, independent model validations were performed using spatially distributed estimates of 1 km ET and cloud-free LST from MODIS (Table 2), as well as aircraft-based soil moisture retrievals from 2D-STAR for five dates over a limited area shown in Figure 1d. The large spatial extent of these remote sensing products helps to further evaluate model performance across different soil and land cover classes in the study region.

2.6. Model Intercomparison With Other Land Surface Models

We also conducted model intercomparisons with a set of coarser resolution LSM outputs from NLDAS-2 [*Mitchell et al*., 2004], referred to here as NLDAS-Noah [*Chen et al*., 1996; *Ek et al*., 2003], NLDAS-Mosaic [*Koster and Suarez*, 1992, 1994], and NLDAS-VIC [*Liang et al*., 1994; *Wood et al*., 1997]. The Noah and Mosaic models were both developed in the coupled climate modeling community and focus on simulating fluxes between the land surface and atmospheric boundary layer [*Xia et al*., 2012]. In contrast, the VIC model was initially developed for macroscale hydrologic simulations [e.g., *Livneh et al*., 2013], with the subdaily energy balance mode implemented in NLDAS. Each offline LSM provides hydrologic outputs at 1/8th degree

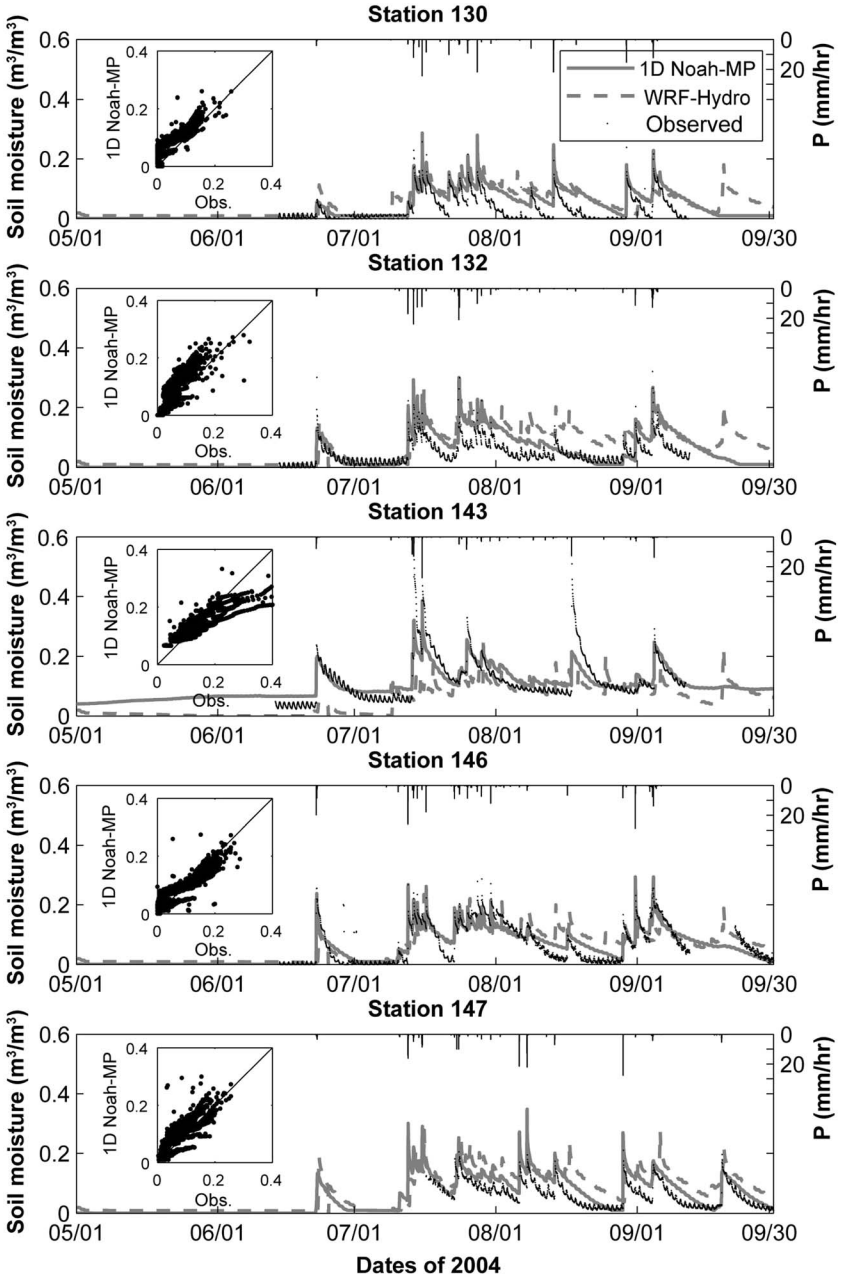

Figure 3. Comparison of surface soil moisture from calibrated 1-D Noah-MP and distributed WRF-Hydro simulations (average over 0–10 cm depth) to observations (5 cm depth) at five stations during 2004. Insets show scatterplots of 1-D Noah-MP and observed soil moisture and 1:1 line. Data gaps are due to missing observations.

(~12 km), hourly resolution over North America (25 to 53°N, 125 to 67°W). NLDAS LSMs have been validated with various observation networks in the U.S. showing reliable performance in different ecosystems [e.g., *Mo et al*., 2011]. Nevertheless, *Bohn and Vivoni* [2016] discussed several limitations of the NLDAS LSMs in terms of seasonal and annual ET estimates in Mexico, as compared to ground data and a process-based modeling effort. These include a lack of ET in irrigated areas for the three NLDAS LSMs and a lack of soil evaporation process in NLDAS-VIC. To our knowledge, an evaluation of the NLDAS LSMs with respect to the surface energy fluxes and their diurnal cycle has not been performed during the NAM. As a result, the comparison of the distributed WRF-Hydro simulations to the NLDAS LSMs will provide insights on the improvements achieved via the enhanced model resolution and process representation with respect to the estimation of land surface

states and fluxes. In this intercomparison, another set of WRF-Hydro simulations is conducted using the original NLDAS forcings to eliminate any possible impact from varying meteorological forcings among the cases.

3. Results and Discussion

3.1. Model Performance at Regional Stations and EC Tower

As a first step toward evaluating the performance of the WRF-Hydro modeling system, we present comparisons between observed (5 cm depth) and simulated (average over 0–10 cm depth) surface soil moisture at five individual stations in Figure 3 during their respective calibration periods (Table 1). A more detailed model performance assessment in terms of surface soil moisture is shown in Table 5 for all stations during calibration and validation periods. We utilize the bias (*B*), Pearson's correlation coefficient (CC), and root-mean-square error (RMSE) to quantify model performance. In addition to illustrating the performance of the 1-D Noah-MP simulations, we also present the soil moisture time series extracted from the distributed WRF-Hydro simulation (with the routing option turned on) 1 km output at the station locations in Figure 3. Both the 1-D Noah-MP and the distributed WRF-Hydro simulations use calibrated soil parameters. Overall, the 1-D Noah-MP simulations are capable of capturing the observed soil moisture response to precipitation and the recession behavior during interstorm periods at the five stations selected to represent different soil and vegetation types. For the five stations used in the model calibration, the 1-D Noah-MP simulations show a better performance with lower *B* (0.016 ± 0.010 m^3/m^3), higher CC (0.861 ± 0.030), and relatively lower RMSE (0.037 ± 0.005 m^3/m^3), as compared to 1-D simulations with the default soil parameters in the current WRF-Hydro release (not shown, $B = 0.092 \pm 0.039$ m^3/m^3, $CC = 0.746 \pm 0.090$, $RMSE = 0.110 \pm 0.027$ m^3/m^3). The improvements in simulating soil moisture are achieved from calibration of the pore size distribution index (*B* parameter), which was identified as the most sensitive parameter. The 1-D model performance is slightly degraded during the validation period, with *B* of 0.008 ± 0.021 m^3/m^3, CC of 0.581 ± 0.201, and RMSE of 0.057 ± 0.014 m^3/m^3. In comparison, the distributed 1 km WRF-Hydro simulations, with the routing option turned on (routing) and off (nonrouting), match the soil moisture observations to a lesser degree. Across all locations, the distributed WRF-Hydro simulations (routing) exhibited a low *B* (0.017 ± 0.035 and -0.010 ± 0.037 m^3/m^3 for calibration and validation periods), comparable to the 1-D Noah-MP cases. However, a small increase is observed in RMSE (0.063 ± 0.009 and 0.063 ± 0.021 m^3/m^3) and a lower (higher) CC is obtained for calibration (validation) periods (i.e., 0.556 ± 0.053 and 0.659 ± 0.21) as compared to the 1-D Noah-MP cases. Comparisons between the routing and nonrouting simulations reveal the relatively low impact of surface and subsurface routing on the soil moisture redistribution across all stations. Since soil and vegetation classes and parameters are consistent in the 1-D and distributed cases, their differences in simulated soil moisture are primarily due to the varying precipitation forcings since rain gauge data (bias-corrected NLDAS) are used in the 1-D (distributed) model runs. For example, seasonal differences of −29, 31, 129, −19, and 16 mm were found between the precipitation products at the five stations (stations 130, 132, 143, 146, and 147) shown in Figure 3.

We also evaluated the 1-D Noah-MP simulations against turbulent flux measurements at station 147 during 2004. Unfortunately, the EC tower at station 147 had no flux data for 2013, thus limiting the possible comparisons. Figure 4 compares the 1-D Noah-MP simulations with observed latent (λE) and sensible (*H*) heat flux measurements in a number of different ways. Time series comparisons of hourly simulations and observations indicate that the magnitudes of λE and *H* are captured well during the period of 23 July to 30 September 2004, in particular the increase (decrease) of latent (sensible) heat flux during rainfall events (Figures 4a and 4b). Model performance is similar to the results of *Vivoni et al*. [2010] and *Méndez-Barroso et al*. [2014] at station 147 using the tRIBS distributed hydrologic model [*Ivanov et al*., 2004]. Scatterplots of the observed and simulated turbulent fluxes shown in Figures 4c and 4d show a high CC of 0.76 and low RMSE of 62 W/m^2 for λE but a poorer fit for *H*, with CC of 0.26 and RMSE of 439 W/m^2. For comparison, the metrics with default soil parameters are CC = 0.42 and RMSE = 71 W/m^2 for λE and CC = 0.20 and RMSE = 439 W/m^2 for *H*. Lower model performance for *H* is attributed to several days immediately after storm events where the 1-D Noah-MP simulations overestimate *H*. If we exclude these days in July and August (23 July to 15 August), an improved set of metrics is obtained (CC = 0.82

Table 5. Model Performance Metrics for Surface Soil Moisture (5 cm Depth) From Calibrated 1-D Noah-MP Simulations and Distributed WRF-Hydro Simulations With the Routing Option Turned On and Off: Bias (B), Correlation Coefficient (CC), and Root-Mean-Square Error (RMSE), Defined in *Mascaro et al.* [2015][a]

	Calibration								
	1-D Noah-MP			Distributed WRF-Hydro (Routing)			Distributed WRF-Hydro (Nonrouting)		
Station	B (m^3/m^3)	CC (–)	RMSE (m^3/m^3)	B (m^3/m^3)	CC (–)	RMSE (m^3/m^3)	B (m^3/m^3)	CC (–)	RMSE (m^3/m^3)
130	0.030	0.831	0.040	0.035	0.518	0.058	0.034	0.529	0.053
132	0.023	0.845	0.041	0.044	0.585	0.066	0.042	0.593	0.060
143	0.004	0.891	0.039	−0.047	0.494	0.078	−0.049	0.493	0.081
146	0.004	0.903	0.029	0.010	0.644	0.052	0.008	0.663	0.049
147	0.020	0.834	0.035	0.043	0.537	0.063	0.042	0.504	0.060
Mean	0.016	0.861	0.037	0.017	0.556	0.063	0.015	0.557	0.061
SD	0.010	0.030	0.005	0.035	0.053	0.009	0.035	0.064	0.011
	Validation								
	1-D Noah-MP			Distributed WRF-Hydro (Routing)			Distributed WRF-Hydro (Nonrouting)		
Station	B (m^3/m^3)	CC (–)	RMSE (m^3/m^3)	B (m^3/m^3)	CC (–)	RMSE (m^3/m^3)	B (m^3/m^3)	CC (–)	RMSE (m^3/m^3)
130	0.015	0.776	0.047	−0.008	0.870	0.049	−0.006	0.864	0.049
131	0.018	0.691	0.051	−0.008	0.825	0.047	−0.007	0.824	0.046
132	0.014	0.733	0.047	−0.008	0.818	0.048	−0.011	0.836	0.046
134	0.005	0.717	0.064	−0.040	0.695	0.073	−0.043	0.696	0.079
137	0.042	0.366	0.085	0.017	0.314	0.079	0.015	0.329	0.076
138	−0.022	0.013	0.080	−0.041	0.109	0.084	−0.043	0.142	0.085
139	0.043	0.304	0.066	0.074	0.384	0.092	0.070	0.356	0.092
140	−0.041	0.416	0.084	−0.066	0.476	0.096	−0.070	0.492	0.100
146	0.007	0.594	0.055	−0.032	0.628	0.074	0.020	0.693	0.079
147	0.008	0.759	0.044	−0.003	0.734	0.043	−0.001	0.714	0.045
150	0.001	0.604	0.053	−0.063	0.762	0.084	−0.061	0.762	0.082
151	−0.004	0.610	0.057	−0.067	0.790	0.088	−0.066	0.771	0.089
156	−0.013	0.563	0.057	0.003	0.622	0.054	0.031	0.679	0.048
158	0.022	0.790	0.045	0.011	0.851	0.032	0.015	0.849	0.034
161	0.010	0.680	0.047	0.021	0.778	0.045	0.022	0.764	0.047
165	−0.002	0.759	0.040	0.011	0.841	0.040	0.011	0.827	0.042
170	0.029	0.500	0.055	0.029	0.696	0.046	0.031	0.679	0.048
Mean	0.008	0.581	0.057	−0.010	0.659	0.063	−0.005	0.663	0.064
SD	0.021	0.201	0.014	0.037	0.210	0.021	0.038	0.203	0.021

[a]Mean and standard deviation (SD) values for all stations are reported.

and RMSE = 105 W/m^2). A similar set of comparisons is obtained with the distributed WRF-Hydro simulations extracted for the station 147 location, with a CC of 0.81 and RMSE of 50 W/m^2 for λE and 0.28 and 274 W/m^2 for H (or 0.85 and 61 W/m^2 when the storm periods are excluded). More importantly, Figures 4e and 4f present a comparison of the diurnal cycle of turbulent fluxes, shown as hourly averaged values (symbols) and ±1 standard deviations (SDs, shaded regions) over the period with sufficient data from 5 August to 30 September 2004 (57 days). From these comparisons, it is clear that the diurnal patterns and magnitudes of the surface energy fluxes are captured well within the 1-D Noah-MP simulation, with comparable results found for the distributed WRF-Hydro case for the extracted location when accounting for the higher precipitation input (16 mm in 2004) from the bias-corrected NLDAS forcing.

3.2. Model Performance for Basin-Averaged Conditions and Spatial Patterns

Having established the model performance for surface soil moisture and turbulent heat fluxes, we assess the ability of the distributed WRF-Hydro simulations through comparisons with remotely sensed products. Due to the large spatial extent of the RSB, satellite-based data from MODIS at 1 km resolution offer a reasonable means for evaluating the distributed model performance. Figure 5 presents a time series comparison of basin-averaged ET over 8 day intervals and instantaneous (approximately 10:30 A.M. and 10:30 P.M. local time for MODIS Terra and 1:30 P.M. and 1:30 A.M. for MODIS Aqua) LST during 2004 and 2013. In the 8 day sum of

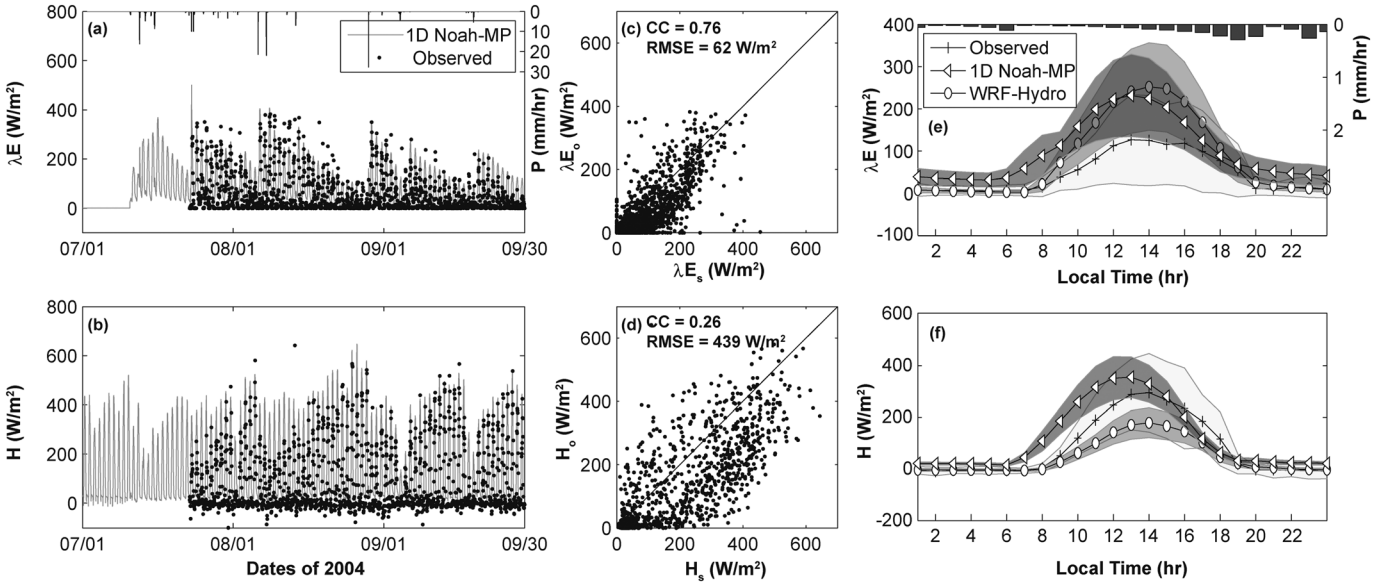

Figure 4. Comparison of latent heat (λE) and sensible heat (H) from 1-D Noah-MP simulation and EC tower observations at station 147 during 2004. (a and b) Time series of hourly values. (c and d) Scatterplots of observed (o) and simulated (s) values, with correlation coefficient (CC), root-mean-square error (RMSE), and 1:1 line shown. (e and f) Diurnal cycles of λE and H, with mean values shown as symbols and shading representing ±1 standard deviation (white for observations, dark gray for 1-D Noah-MP, and light gray for WRF-Hydro).

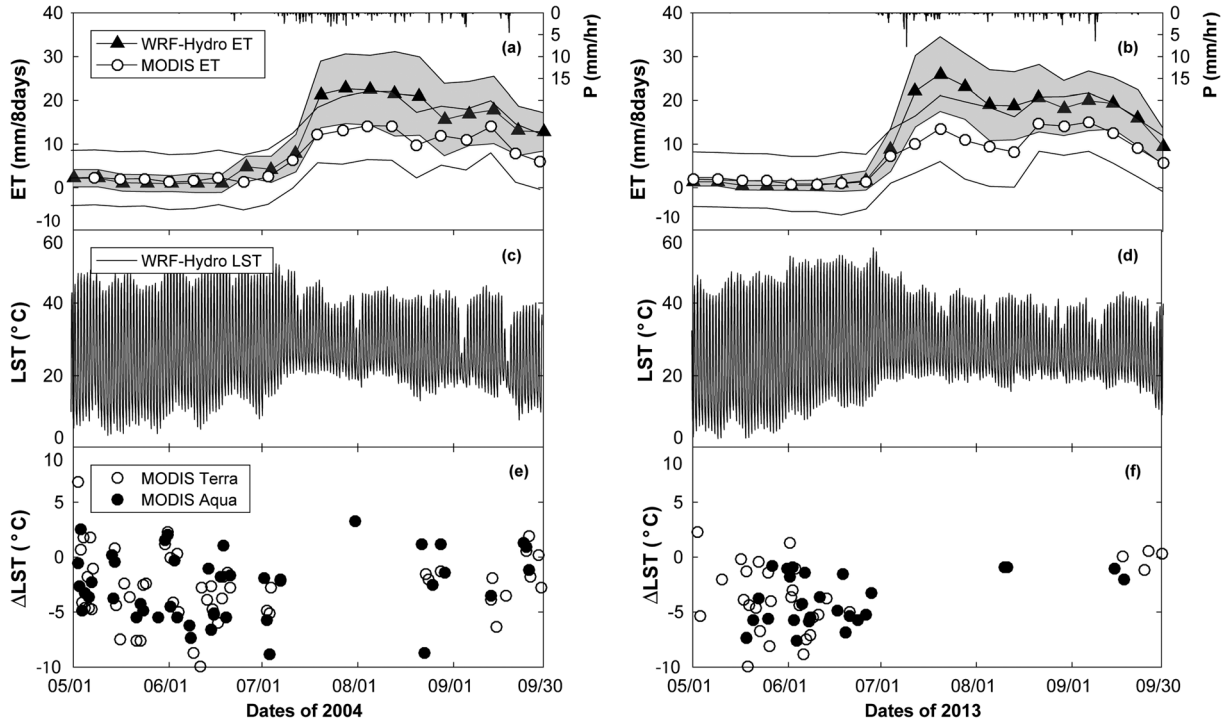

Figure 5. (top row) Comparison of MODIS ET (8 days) to distributed WRF-Hydro simulations during (a) 2004 and (b) 2013. The solid lines represent basin-averaged values, and the shaded areas depict ±1 spatial standard deviation (dark gray for WRF-Hydro ET and light gray for MODIS ET). Basin-averaged precipitation is plotted on the inverted y axis. (middle row) WRF-Hydro simulated basin-averaged LST and its (bottom row) difference to MODIS LST at overpass time (ΔLST, WRF-Hydro–MODIS) during (c and e) 2004 and (d and f) 2013.

Table 6. Model Performance Metrics for Distributed WRF-Hydro Simulations as Compared to Cloud-Free MODIS LST and 2D-STAR Soil Moisture Products at Coincident Times[a]

LST in 2004				
Product/Overpass	*B* (°C)	CC (–)	RMSE (°C)	No.
Terra/day	−1.28	0.77	3.37	29
Terra/night	−4.29	0.61	5.17	24
Aqua/day	−2.41	0.7	4.22	29
Aqua/night	−2.88	0.65	4.49	12
Mean	−2.72	0.68	4.31	23.50
SD	1.08	0.06	0.64	6.95
LST in 2013				
Product/Overpass	B (°C)	CC (–)	RMSE (°C)	No.
Terra/day	−1.75	0.77	3.22	20
Terra/night	−5.04	0.57	6.4	13
Aqua/day	−3.86	0.61	4.95	15
Aqua/night	−3.25	0.57	4.43	11
Mean	−3.48	0.63	4.75	14.75
SD	1.19	0.08	1.14	3.34
Soil Moisture in 2004				
Date	B (m^3/m^3)	CC (–)	RMSE (m^3/m^3)	
7 Aug	0.052	0.047	0.070	
8 Aug	0.073	0.085	0.090	
24 Aug	0.052	0.034	0.066	
25 Aug	0.049	0.210	0.072	
26 Aug	0.064	−0.184	0.084	
Mean	0.058	0.039	0.076	
SD	0.009	0.128	0.009	

[a]Statistics of LST products are averaged over all cloud-free days.

ET (Figures 5a and 5b), the spatial average and the ±1 spatial SD over the RSB are depicted by symbols and shaded areas, respectively. For clarity, the WRF-Hydro simulated LST time series is presented in Figures 5c and 5d, while ΔLST (WRF-Hydro–MODIS) at MODIS overpass times is shown in Figures 5e and 5f. Although the land cover classifications used in WRF-Hydro and in the MODIS ET products are slightly different (USGS 24 category versus MODIS 21 category), comparisons of the basin-averaged ET indicate that the distributed WRF-Hydro simulations and MODIS product exhibit negligible values prior to the arrival of monsoon rain events in July. WRF-Hydro captures the seasonal evolution of ET well, with maximum basin-averaged values near 20 mm per 8 days (2.5 mm/d), depending on the precipitation distribution and vegetation response for each season. This comparison is consistent with *Bohn and Vivoni* [2016], who found that MODIS 8 day products underestimate ET during the NAM as compared to ground observations and other model-derived products. Factors that could contribute to the inconsistency between MODIS ET estimates and ground data include scale differences, uncertainty in the input meteorological data, limitations of the algorithm in representing biophysical processes, and parameterizations of the underlying MODIS ET model. The underestimation of MODIS ET product has also been found in other dry ecosystems, with errors ranging from 2 to 7 mm per 8 days [e.g., *Ramoelo et al.*, 2014; *Jovanovic et al.*, 2012]. As a result, the distributed WRF-Hydro simulations are considered to adequately represent the basin-averaged ET in the RSB, thus increasing model confidence from the scale of an individual EC tower (Figure 4) to the more varied ET conditions in the basin.

In terms of the basin-averaged LST (Figures 5c and 5d), the distributed WRF-Hydro simulation represents well the seasonal evolution occurring during the NAM characterized by the cooling of the land surface in response to increased cloud cover and soil water availability, as documented by *Xiang et al.* [2014]. To compare the basin-averaged LST between WRF-Hydro simulations and MODIS products, their differences

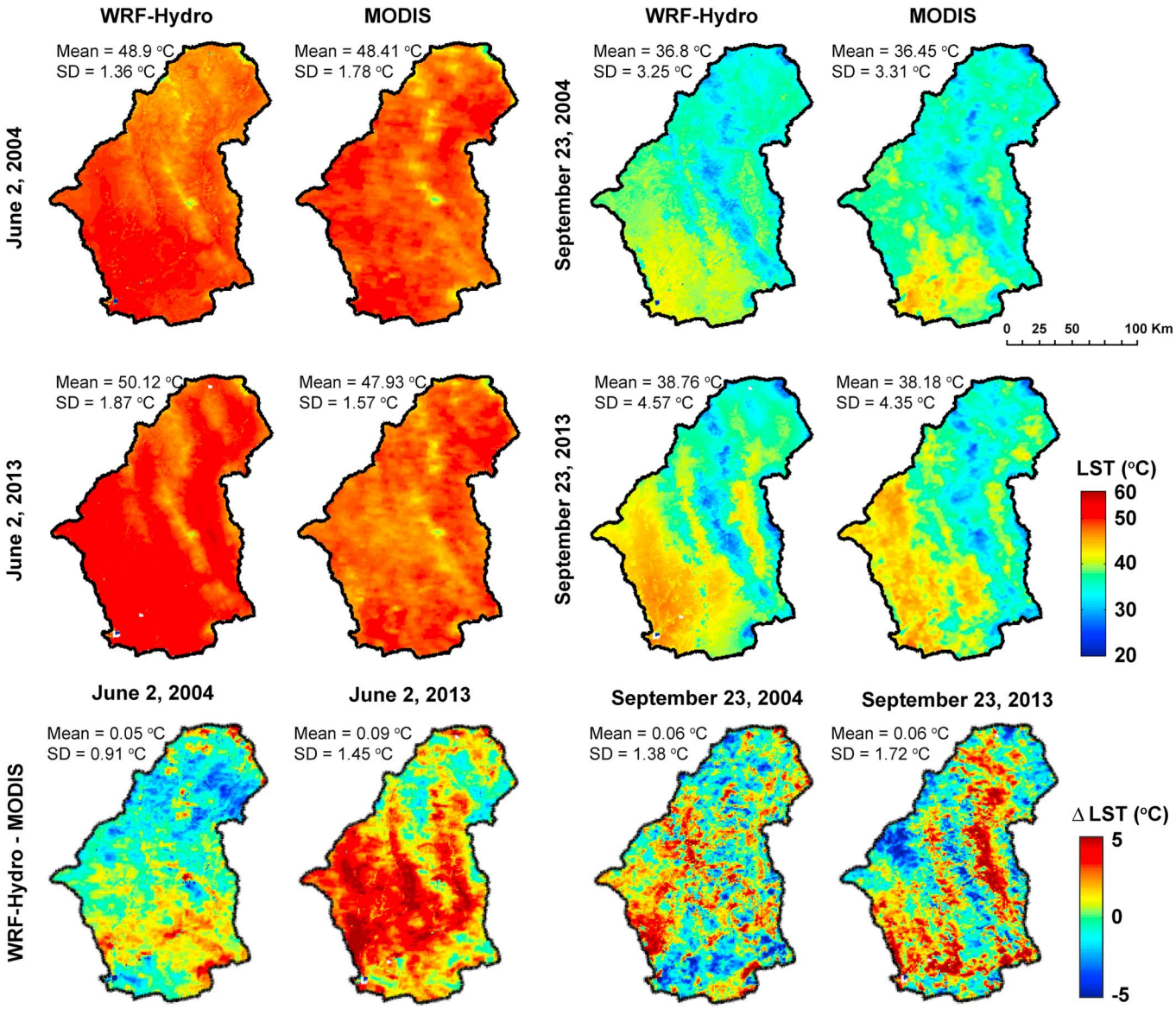

Figure 6. Comparison of MODIS LST to distributed WRF-Hydro simulations on 2 June and 23 September for each year (2004 and 2013) at overpass time of 10:30 A.M. Basin-averaged (mean) and spatial standard deviation (SD) values are shown for each case. (bottom row) The plots present LST difference between WRF-Hydro and MODIS.

(WRF-Hydro–MODIS) are plotted in Figures 5e and 5f. At most of the overpass times, the WRF-Hydro simulations have absolute errors lower than 5°C. Quantitative comparisons between MODIS LST and WRF-Hydro simulations are presented in Table 6 for daytime (10:30 A.M. for Terra and 1:30 P.M. for Aqua) and nighttime overpasses (10:30 P.M. for Terra and 1:30 A.M. for Aqua) during cloud-free days (number of days reported in Table 6). WRF-Hydro hourly outputs are linearly interpolated to the MODIS overpass times, a process that can introduce error in the comparison. The spatial patterns of LST are represented properly in the distributed WRF-Hydro simulations, with a high CC of 0.68 ± 0.06 and 0.63 ± 0.08 and a low RMSE of 4.31 ± 0.64°C and 4.75 ± 1.14°C in 2004 and 2013, respectively. The differences in spatial variability between WRF-Hydro outputs and MODIS LST images are mainly resulted from uncertainties in model forcings at the MODIS overpass time.

To further explore the spatial comparisons, Figure 6 presents the daytime LST patterns obtained from the distributed WRF-Hydro simulation at the coincident time of the MODIS Terra daytime overpass for two

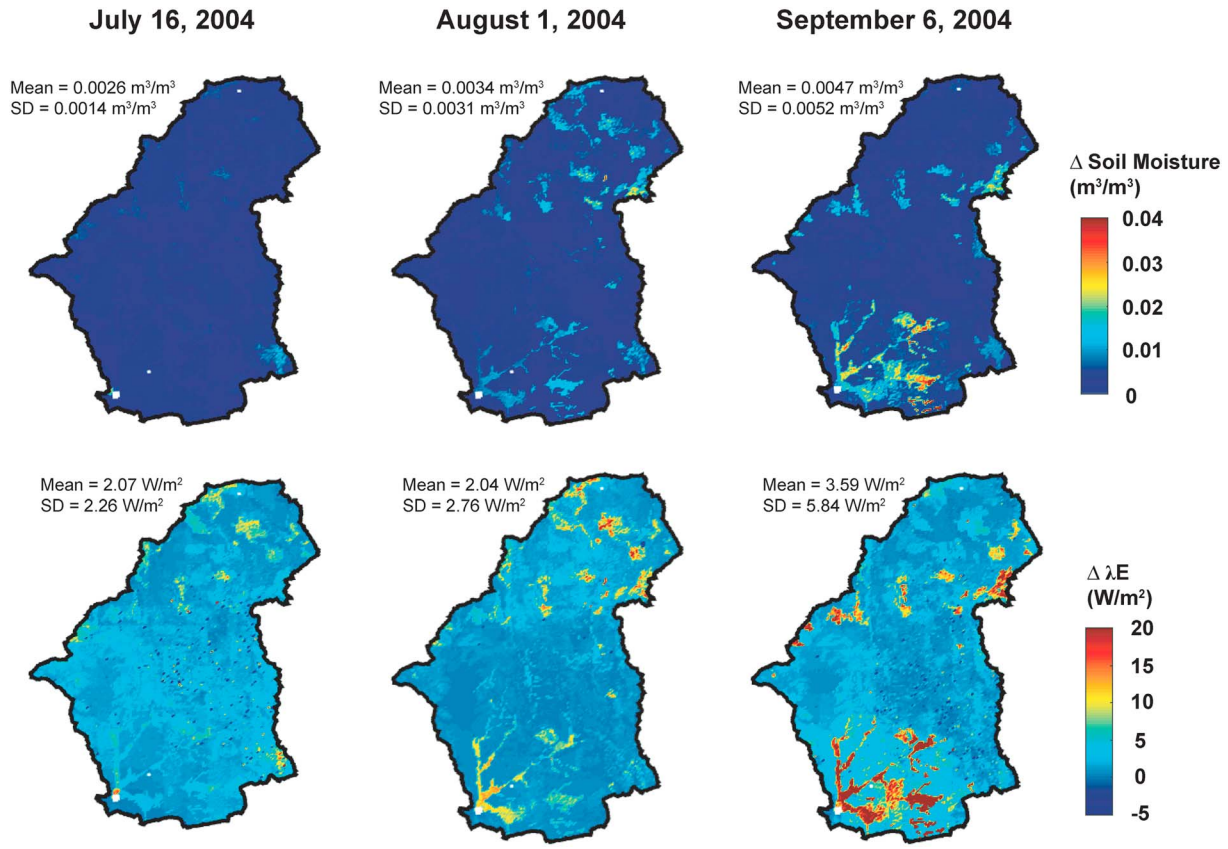

Figure 7. Spatial distribution of the difference (Δ) in (top) surface soil moisture and (bottom) latent heat flux between WRF-Hydro with routing option turned on and off (routing minus nonrouting) at noon (12:00 P.M.) on three selected dates after storm events were observed in the basin: 16 June, 1 August, and 6 September 2004. Basin-averaged (mean) and spatial standard deviation (SD) values of Δ are shown for each case.

dates (2 June and 23 September) of each summer period, along with their differences (WRF-Hydro–MODIS). These two dates are selected to represent premonsoon and monsoon condition, while avoiding cloudy weather conditions. From June to September, basin-averaged LST decreases in a similar fashion in WRF-Hydro (−12.10°C and −11.36°C) as compared to MODIS (−11.96°C and −9.75°C) for 2004 and 2013, respectively. In addition, a similar increase is noted in the spatial variability of LST as captured by the spatial SD (+1.89°C and +1.53°C in 2004; +2.70°C and +2.78°C in 2013) in the distributed WRF-Hydro simulations and MODIS product. An excellent correspondence is observed between simulated and remotely sensed images (both at 1 km resolution) with spatial means of the difference maps lower than 0.25°C and standard deviations lower than 2°C. The ability of the distributed WRF-Hydro simulations to represent cooler conditions at higher elevations and the warmer surfaces in coastal plains in the southern part of the RSB are noteworthy. While only four overpasses are presented with maps, all the cloud-free images are used to derive statistics reported in Table 6.

The impact of the surface and subsurface routing scheme carried out on a nested 100 m grid is presented in Figure 7 through difference maps from two distributed WRF-Hydro simulations (routing minus nonrouting). The difference maps show the surface soil moisture (in m^3/m^3) and latent heat flux (λE in W/m^2) at noontime for three selected dates in 2004 after the occurrence of storm events in the RSB. As expected, WRF-Hydro with the fine-resolution routing on redistributes soil moisture and affects the spatial distribution of latent heat flux, especially in the riparian or floodplain zone near the basin outlet. However, it should be noted that the magnitudes of these differences are relatively small (i.e., 0.01 to 0.04 m^3/m^3) and last only for short periods of time (i.e., 2 to 3 days) after individual storm events [*Vivoni et al.*, 2007]. Given the relatively minor impact of the fine-resolution routing on the distributed WRF-Hydro simulations in the RSB (as reported in Table 5 and Figure 7), the influence of lateral soil moisture redistribution on the spatial patterns of the surface energy

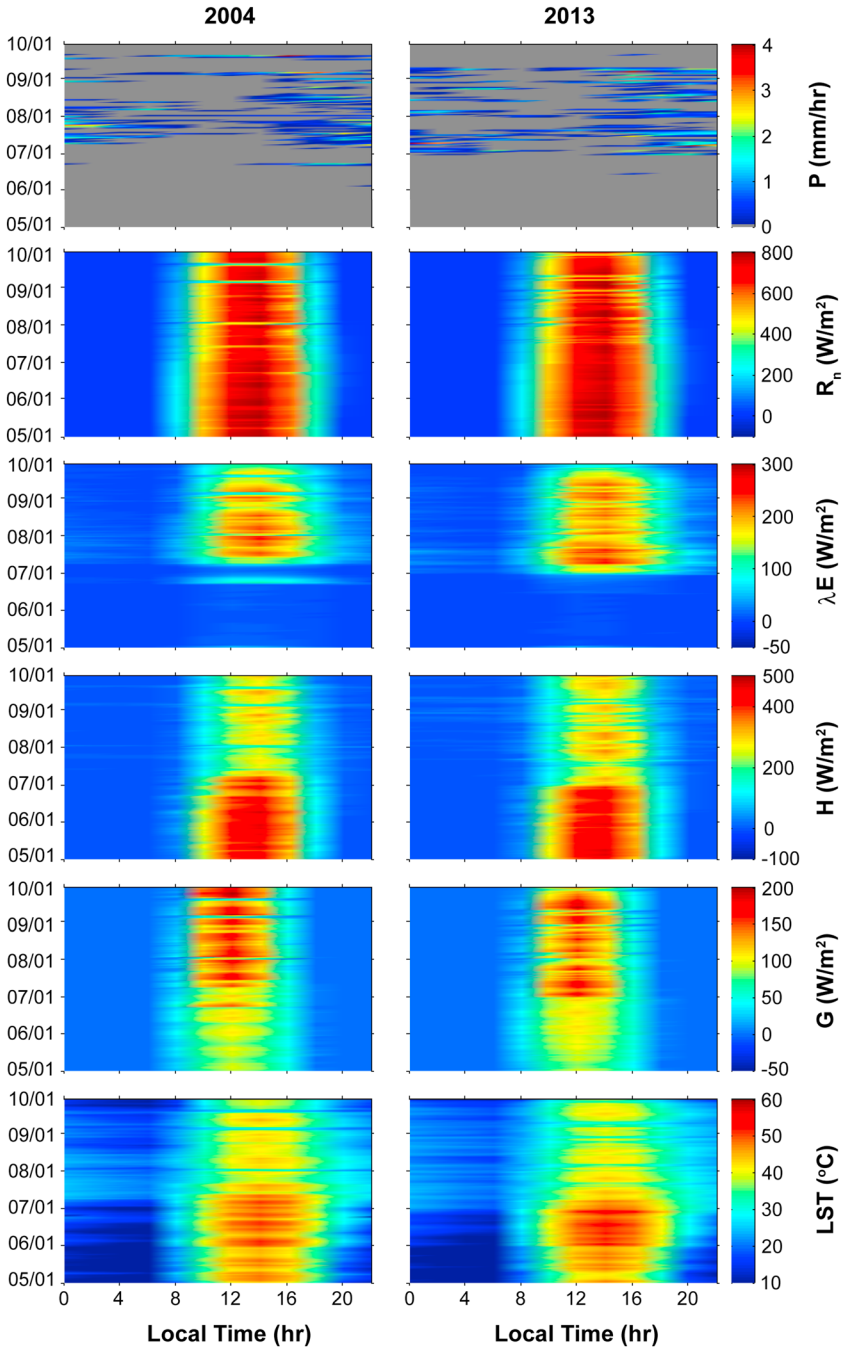

Figure 8. Diurnal cycles of basin-averaged precipitation (P), surface energy fluxes (R_n, λE, H, and G), and LST from May to September (hourly values in local time for each day) in 2004 and 2013. Precipitation is from bias-corrected NLDAS (gray colors depict $P = 0$), while other variables are from distributed WRF-Hydro simulations (colors depict magnitude of variable).

fluxes is considered to be small, and subsequent analyses are focused on the distributed WRF-Hydro simulations without routing.

As a final measure of the spatial performance of the WRF-Hydro simulations, Table 6 includes a quantitative comparison to the soil moisture retrievals from the 2D-STAR sensor available for 5 days in 2004. Figure 1d depicts the maximum spatial extent of the 2D-STAR images at 800 m resolution, though gaps in coverage exist depending on the retrieval algorithm [*Ryu et al.*, 2010]. *Mascaro et al.* [2015] compared the 2D-STAR

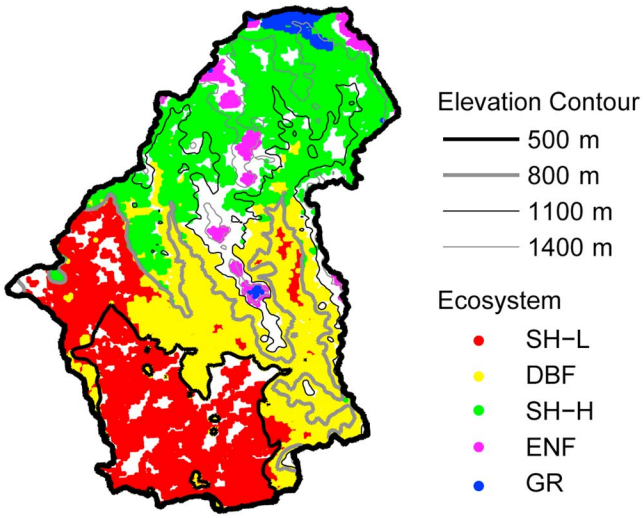

Figure 9. Spatial distribution of five major ecosystems with elevation contours: shrubland lower than 800 m (SH-L, 23.4% of A), deciduous broadleaf forest from 500 to 1000 m (DBF, 24.2% of A), shrubland higher than 800 m (SH-H, 21% of A), evergreen needleleaf forest higher than 1300 m (ENF, 4.2% of A), and grassland higher than 1300 m (GR, 1% of A).

product to the same set of regional stations during the summer of 2004, finding relatively poor performance (B = −0.011 m^3/m^3 and CC = −0.181) in terms of surface soil moisture. Given the uncertainty in the 2D-STAR product, the relatively poor comparisons with distributed WRF-Hydro simulation (B = 0.058 ± 0.009 m^3/m^3, CC = 0.039 ± 0.129, RMSE = 0.076 ± 0.009 m^3/m^3) are not unexpected and in line with those of the effort reported by *Mascaro et al.* [2015] with tRIBS. Considering that the 2D-STAR product covers 24% of the RSB, it is suitable to assess the model spatial performance with respect to soil moisture, despite the limitations of the retrieval. In addition, the simulation correspondence to soil moisture observations at a number of regional stations suggests that the spatial patterns are more adequately captured than what is indicated by the comparison to the 2D-STAR product. Although uncertainties in MODIS ET and 2D-STAR soil moisture inhibit further model evaluation, the distributed performance of WRF-Hydro has been more thoroughly corroborated with respect to readily available, and reasonably confident, LST observations. Over arid to semiarid regions, LST is strongly related to soil moisture availability, which controls the spatial distribution and diurnal cycle of ET, and other surface energy fluxes, as explored next.

3.3. Diurnal Cycle of Surface Energy Fluxes Across Different Ecosystems

To provide context on the diurnal cycle of the surface energy fluxes, we first explore the seasonal evolution of basin-averaged conditions in Figure 8 with respect to precipitation (P), net radiation (R_n), latent heat flux (λE), sensible heat flux (H), ground heat flux (G), and land surface temperature (LST). As in prior analyses, basin-averaged conditions are based on aggregations of the distributed WRF-Hydro simulations at 1 km resolution in the RSB. Hourly variations are shown from 1 May to 30 September during 2004 and 2013. Observed precipitation events in the bias-corrected NLDAS forcing exhibit preferential occurrences ranging from the late afternoon to nighttime, consistent with prior studies in the region [e.g., *Gebremichael et al.*, 2007; *Gochis et al.*, 2007; *Mascaro et al.*, 2014]. Interesting features of the North American monsoon are apparent in the diurnal cycle of precipitation in Figure 8, including intensity variations that have been shown to be related to the occurrence of gulf surges and mesoscale convective complexes [e.g., *Schiffer and Nesbitt*, 2012; *Seastrand et al.*, 2015]. Moreover, the monsoon onset in early July leads to a dramatic shift in the diurnal shape and overall magnitude of surface energy fluxes, with an observed reduction (increase) in R_n and H (λE and G). *Méndez-Barroso and Vivoni* [2010] documented similar trends at the EC tower (station 147) based on observed surface fluxes during 2004. The increase in G after monsoon onset is mainly resulted from the changes in thermal properties under wet conditions. Of importance is that a reduced amount of available energy (R_n-G) after the monsoon onset is partitioned into a higher fraction of latent heat as opposed to sensible heat flux, which leads to a cooling of the land surface (i.e., a significant reduction in LST). As expected, the diurnal cycle of the turbulent fluxes is strongly controlled by net radiation, with modulations occurring for days with precipitation events, including higher λE in early mornings and afternoons and lower nighttime LST values, when soil moisture is present within the RSB.

To further analyze the diurnal cycles, we identify five ecosystems occurring in different elevation bands in Figure 9. These ecosystems occupy 73.8% of the total area (A) of RSB and occur in contiguous subregions,

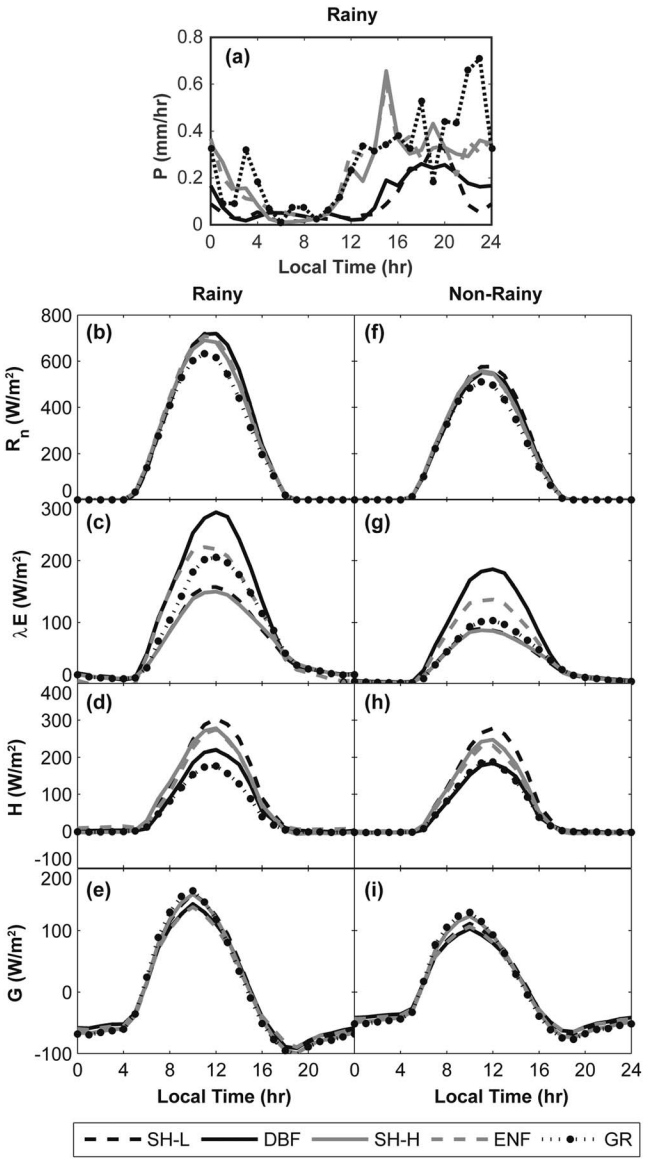

Figure 10. Time-averaged diurnal cycles of precipitation (*P*) and surface energy fluxes (R_n, λE, *H*, and *G*) from distributed WRF-Hydro simulations averaged within each ecosystem (SH-L, DBF, SH-H, ENF, and GR) for rainy and nonrainy days from July to September in 2004 and 2013. The numbers of rainy days for the five ecosystems are 40, 46, 41, 46, and 40, while the numbers of nonrainy days are 52, 46, 51, 46, and 52. A day is defined as 00:00 to 23:59 local time.

with SH-L present shrubland at low elevations (<800 m) to the south and east; deciduous broadleaf forest (DBF) found at midelevations (500 to 1000 m) in the central and western areas; shrubland at elevations higher than 800 m (SH-H) in the north and west; and evergreen needleleaf forest (ENF) and grassland (GR) occupying the highest elevations (>1300 m) in mountain areas. The plant rooting depths of SH-L, SH-L, and GR are 1 m, while DBF and ENF have rooting depths of 2 m. Based on this classification, Figure 10 presents the diurnal cycle of precipitation (*P*) and surface energy fluxes (R_n, λE, *H*, and *G*) for each ecosystem, averaged during July to September (JAS) for both years. To isolate the impact of soil moisture conditions, the distributed WRF-Hydro simulations were categorized into rainy and nonrainy (or wet and dry) days using a mean areal precipitation threshold of 5 mm/d as a proxy for soil wetness. A rainy day was determined if the threshold was exceeded on the day prior to the analysis given that 5 mm/d is an ecologically effective rainfall amount, above which desert ecosystems will generally exhibit responses to rainfall [*Ogle and Reynolds*, 2004]. This threshold is applied to the five ecosystems on a daily basis. The mean diurnal cycles of *P* for each ecosystem are presented in Figure 10a, which shows higher rainfall rates in high-elevation ecosystems (SH-H, ENR, and GR). Classifying the surface energy fluxes using the major ecosystems and daily wetness conditions highlights a few interesting features. For instance, the mean diurnal cycle of R_n and *G* are not substantially different among ecosystems, despite variations in elevation and vegetation properties, with the exception of lower R_n for grasslands. More interesting are the higher R_n and *G* observed during rainy days, which behave similarly to the observations in *Eltahir* [1998] and are analyzed locally by *Méndez-Barroso and Vivoni* [2010]. Essentially, wet soil moisture conditions along with increased vegetation greenness reduce surface albedo, leading to a higher R_n. During rainy days in JAS, the land surface receives a higher amount of available energy (R_n-*G*) of nearly 116 W/m^2 as compared to nonrainy days, with negligible differences between ecosystems. Nevertheless, the available energy is partitioned into turbulent fluxes in varying ways depending strongly on local vegetation and elevation. Among the five ecosystems, DBF exhibits the highest λE, while SH-L has the largest peak value of *H*, indicating that the magnitude and

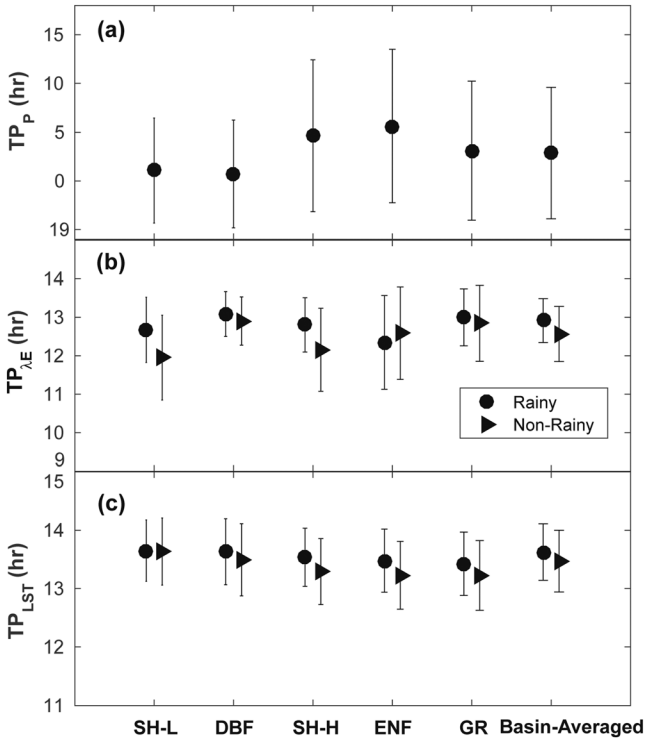

Figure 11. Time of peak (TP) of *P*, λE, and LST within each ecosystem (SH-L, DBF, SH-H, ENF, and GR) and over the entire basin (basin-averaged) for rainy and nonrainy days from July to September in 2004 and 2013. Average (symbols) and standard deviation (vertical bars) values are shown for each case.

timing of diurnal turbulent fluxes can vary for ecosystems in close proximity. Given the relatively high precipitation amount over DBF, the impact of low soil water stress on transpiration through stomatal control is the main responsible factor for its high λE, even though DBF can also uptake deeper root zone soil moisture. The effects of wetness appear to be stronger for λE as compared to *H*, with the shapes of the turbulent flux diurnal cycles also being sensitive to the classification into rainy and nonrainy days.

To summarize these findings, Figure 11 compares the timing of the diurnal peak of *P*, λE, and LST for the different ecosystems and wetness conditions. For comparison, results for the entire basin are also plotted. While the mean diurnal peak of precipitation (TP_P) falls after midnight (symbols), the large standard deviations (vertical bars) indicate that this is due to sampling a wide range of occurrences (Figure 8). Small differences in precipitation timing are apparent between lower elevation ecosystems (SH-L and DBF, see Figure 9 for reference) and higher elevation sites (SH-H, ENF, and GR), in a fashion consistent with observations [*Gochis et al*., 2007; *Nesbitt et al*., 2008]. As noted previously, the mean time of diurnal peak of latent heat flux ($TP_{\lambda E}$) shows variability among ecosystems and a high sensitivity to rainfall events, though standard deviations are less than 2 h. $TP_{\lambda E}$ occurs earlier for shrublands (SH-L and SH-H) than other ecosystems under nonrainy conditions. For SH-L, SH-H, DBF, and GR, $TP_{\lambda E}$ generally occurs later in time under rainy conditions than for nonrainy conditions. We diagnosed these effects by inspecting the peak diurnal timing of soil evaporation (TP_E) and plant transpiration (TP_T). We found that TP_E had low sensitivity to ecosystem type or wetness conditions, whereas TP_T occurred much earlier for shrublands. This suggests the distributed WRF-Hydro simulations (due to the underlying physics in Noah-MP) reasonably capture ecosystem differences in the physiological controls on λE that are related to stomatal resistance and water stress, as noted in observational studies [e.g., *Goldstein et al*., 2000; *Wilson et al*., 2003]. This difference between ecosystems is mainly due to the soil moisture factor controlling stomatal resistance (β factor) in Noah-MP, which represents interactions between soil water stress and terrestrial ecosystem dynamics. Furthermore, the variation of the diurnal cycles of surface energy fluxes among ecosystems induces small changes in TP_{LST}, with slightly earlier peaks occurring during nonrainy periods and for higher elevation sites (SH-H, ENF, and GR).

3.4. Spatial Distribution of Diurnal Signatures of Precipitation and Evapotranspiration

The spatial signatures of the diurnal cycle of precipitation and surface energy fluxes are useful tools to understand the influence of terrain, soil, and vegetation features captured in the distributed WRF-Hydro simulations. For reference, Figure 12 presents the spatial distribution of the total precipitation (*P*), number of rainy days, and the mean diurnal peak timing of precipitation (TP_P) for JAS periods in 2004 and 2013, which are derived from the bias-corrected NLDAS forcings. Precipitation totals reflect a longitudinal variation that is related to the higher elevations in eastern areas, as noted by *Gochis et al*. [2007], and are due to an increase in

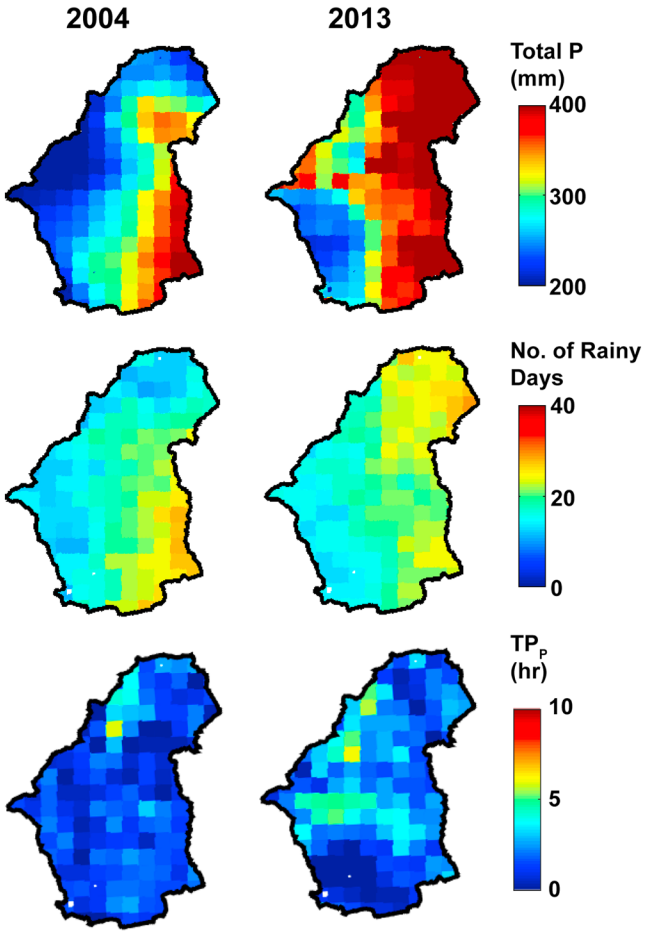

Figure 12. Spatial distribution of (top) total *P* (mm), (middle) number of rainy days, and (bottom) time of peak *P* (h) averaged for all rainy days from July to September in 2004 and 2013.

the number of rainy days during each period. TP_P varies considerably in space and between the 2 years. Nevertheless, the spatial pattern of TP_P follows the conceptual model of *Nesbitt et al*. [2008] in that mountain ranges tend to show a precipitation peak near midnight, while lower valleys exhibit TP_P occurring after midnight. This pattern is indicative of the formation, upscale organization, and movement of mesoscale convective complexes from mountain regions toward lower elevation areas. Based on the prior discussion, we would expect that the spatial variations of *P* and TP_P influence the diurnal cycle of evapotranspiration to some extent.

The spatial patterns of the mean diurnal peak timing of latent heat flux ($TP_{\lambda E}$), plant transpiration (TP_T), and soil evaporation (TP_E), along with the mean peak values, are presented in Figure 13 for rainy and nonrainy days in JAS during 2004 and 2013. Regions occupied by DBF and ENF that receive comparatively abundant rainfall exhibit the highest peak values of λE, consistent with the mean diurnal cycles of each ecosystem shown in Figure 10. These areas are clearly isolated in the spatial distributions by exhibiting peak λE of 200 W/m^2 (dark red) and peak *T* ranging from 0.3 to 0.5 mm/h (yellow to red) for both rainy and nonrainy days. This pattern supports that findings by *Méndez-Barroso and Vivoni* [2010] and *Méndez-Barroso et al*. [2014] that intermediate to high elevation ecosystems are the primary ET sources in the region, mainly due to the large rainfall amount and their high transpiration in response to water availability. In comparison, peak *E* is relatively low and associated with soil properties, with higher peak *E* in clay valley soils. In contrast to *P*, the distributions of vegetation and soil properties play a smaller role on the peak timing of evapotranspiration and its components, in particular for nonrainy days. When the prior day had sufficient precipitation, $TP_{\lambda E}$ is modified substantially, with delayed peak occurrences in the RSB attributed to TP_T since TP_E is insensitive to wetness. Close inspection of TP_T reveals that rainy days have a delayed diurnal cycle in shrublands (SH-L and SH-H), which are under higher water stress than DBF and ENF areas. Furthermore, the spatial pattern of TP_T during rainy days bears resemblance to the peak timing of precipitation (TP_P) for each year. This suggests that the diurnal cycle of precipitation is critical for delaying the diurnal peak of plant transpiration in ecosystems that are released from water stress. As a result of this evidence, we find that nighttime storms increase available soil water in water-stressed ecosystems, thus allowing for a higher and more sustained ET during the subsequent day and accelerating the return of moisture to the atmosphere.

3.5. Comparison of Surface Energy Fluxes in Other Land Surface Models

We compared the extent to which one-dimensional NLDAS LSMs capture the spatiotemporal dynamics of the diurnal cycle of surface energy fluxes obtained in the distributed WRF-Hydro simulations. Comparisons of

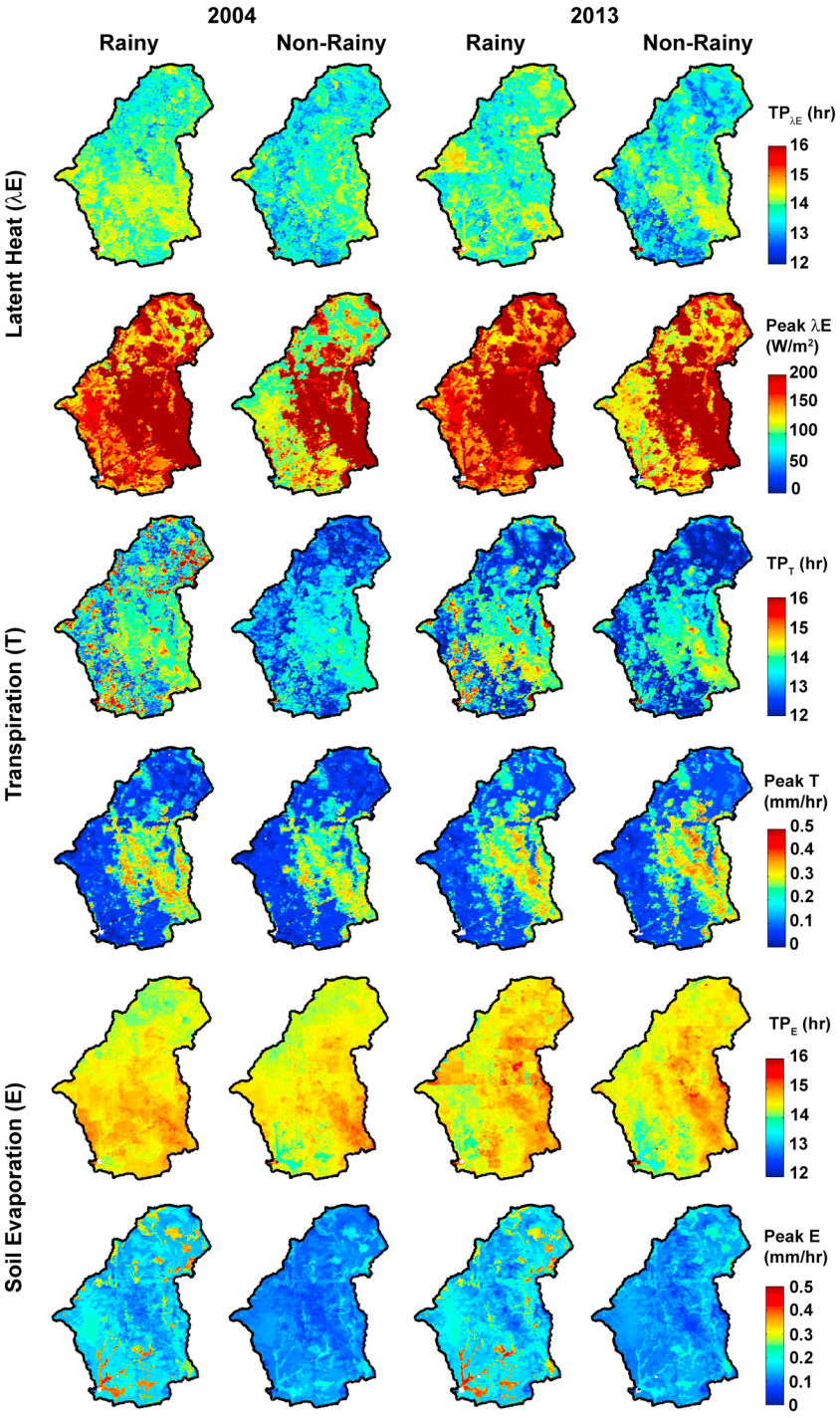

Figure 13. Spatial distribution of the time of peak (TP) and peak value of λE, T, and E for rainy and nonrainy days from July to September in 2004 and 2013.

the seasonal evolution of the diurnal cycle of λE revealed that all NLDAS LSMs capture the transition during the monsoon onset (not shown). NLDAS-Mosaic and NLDAS-Noah exhibit earlier diurnal peak times, and NLDAS-VIC had a weaker diurnal cycle with lower ET rate (not shown). The relative importance of deciduous (DBF) and shrubland (SH-L and SH-H) ecosystems captured in WRF-Hydro in terms of the peak λE is also preserved in the NLDAS LSMs that have similar land cover classifications. However, the seasonal ratio of ET/P exhibits important differences among the simulations (Table 7). Note that the

Table 7. Basin-Averaged Fluxes From Distributed WRF-Hydro (Original and Bias-Corrected NLDAS Forcing), NLDAS-Noah, NLDAS-Mosaic, and NLDAS-VIC Simulations for 2004 and 2013[a]

	Distributed WRF-Hydro									
	Original NLDAS		Corrected NLDAS		NLDAS-Noah		NLDAS-Mosaic		NLDAS-VIC	
Fluxes (Unit)	2004	2013	2004	2013	2004	2013	2004	2013	2004	2013
P (mm)	245	298	288	383	263	311	263	311	263	311
ET (mm)	211	230	213	232	223	233	235	252	208	210
T (mm)	94	106	89	99	100	110	70	90	131	133
E (mm)	104	109	112	117	89	92	119	121	0	0
I (mm)	12	15	11	16	34	32	39	37	39	42

[a]Variables (in mm) are precipitation (*P*), evapotranspiration (ET), transpiration (*T*), soil evaporation (*E*), and canopy evaporation (*I*).

WRF-Hydro simulations have consistently lower ET/P (74% in 2004 and 61% in 2013) after bias correction of the NLDAS precipitation. Furthermore, the NLDAS LSMs have large differences in ET partitioning, with an average *T*/ET of 46% (NLDAS-Noah), 33% (NLDAS-Mosaic), and 63% (NLDAS-VIC), as compared to the average *T*/ET of 42% in the bias-corrected WRF-Hydro and the average *T*/ET of 45% in the original WRF-Hydro. This is consistent with *Bohn and Vivoni* [2016], who found significant differences among the NLDAS LSMs in terms of ET/*P* and *T*/ET and attributed these to underlying physical process representations. As expected, the closer correspondence between WRF-Hydro and NLDAS-Noah is primarily due to sharing a partially similar set of physical processes. This result is encouraging for the WRF-Hydro simulations since *Xia et al*. [2015] showed that NLDAS-Noah compared well with a large number of ET observations in the coterminous U.S.

The comparison between the distributed WRF-Hydro simulations and the NLDAS LSMs, all driven by the original NLDAS forcings, is presented in Figure 14 through an analysis of the ecosystem differences in the diurnal cycle of surface energy fluxes between the major ecosystems. We selected the peak diurnal values of latent heat flux (λE) and the plant transpiration and soil evaporation components, expressed in terms of heat flux (λE_T and λE_E in W/m^2), as comparison metrics. Mean differences (color bars and symbols) and standard deviations (vertical bars) are shown between three sets of ecosystems, namely, DBF, SH-H, and SH-L, shown to have substantial variations in diurnal fluctuations and to occur in close proximity. The comparison reveals that the distributed WRF-Hydro simulations depict large spatial differences in peak λE values between deciduous and shrubland ecosystems, which are not captured in the NLDAS LSMs and that these are primarily attributed to distinct diurnal magnitudes of plant transpiration. The large differences between WRF-Hydro and NLDAS LSMs are partially due to their different spatial resolution (1 km versus 12 km). The enhanced model physics (e.g., vegetation parameterization and soil moisture factor controlling stomatal resistance) in WRF-Hydro also contribute to the large spatial heterogeneity. Specifically, a detailed

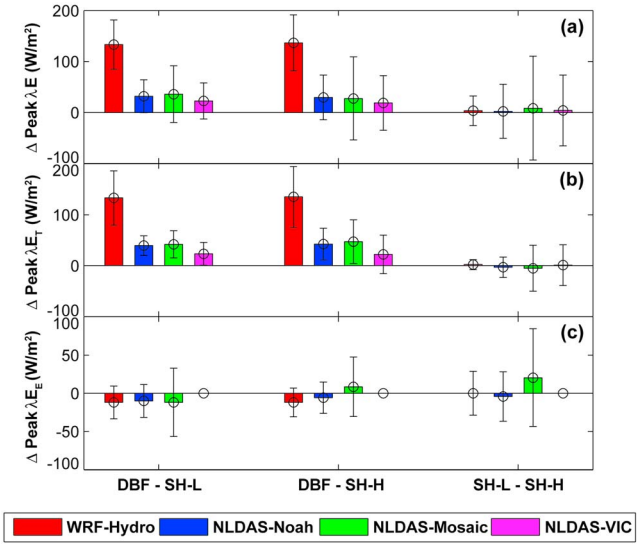

Figure 14. Differences (Δ) in (a) peak λE (latent heat flux), (b) λE_T (plant transpiration), and (c) λE_E (soil evaporation) between ecosystems (DBF minus SH-L, DBF minus SH-H, and SH-L minus SH-H) for WRF-Hydro and NLDAS LSMs. Ecosystem-averaged (color bars) and standard deviation (vertical bars) values are obtained from July to September in 2004 and 2013.

comparison of vegetation parameters used in WRF-Hydro and NLDAS LSMs revealed that rooting depth and stomatal resistance to be the main contributors of their differences: (1) a larger plant rooting depth in WRF-Hydro (2 m for DBF and 1 m for SH-L and SH-H) allows greater access to stored moisture than NLDAS LSMs (1.25 m for DBF and 0.58–0.65 m for SH-L and SH-H) and a larger difference among ecosystems and (2) a lower (dynamic) stomatal resistance in WRF-Hydro (minimum values of 100 s/m for DBF and 300 s/m for SH-L and SH-H) as compared to a static values in NLDAS LSMs that are very similar among ecosystems (175 s/m for DBF and 175–178.9 s/m for SH-L and SH-H). In contrast, spatial differences of peak λE_E between the three ecosystems (Figure 14c) are consistent among WRF-Hydro, NLDAS-Noah, and NLDAS-Mosaic, indicating that these two LSMs represent well the spatial variability in soil evaporation between deciduous and shrubland ecosystems. Since the differences between SH-H and SH-L are small in all cases, the main driver of spatial variability is the distinction between deciduous broadleaf forests with abundant precipitation and shrublands that tend to be under greater water stress. The larger ecosystem differences in λE (~135 W/m^2) in WRF-Hydro, as compared to the NLDAS LSMs (average of ~28 W/m^2), are an indication that the higher resolution and site-specific application of the distributed WRF-Hydro simulations lead to stronger spatial contrasts in ET that have a significant potential to impact simulated atmospheric conditions during the NAM and also have implications on the local recycling of precipitation [e.g., *Dominguez et al*., 2008]. The impacts of these differences on fully coupled, high-resolution atmospheric simulations are the subject of ongoing research.

4. Summary and Conclusions

Despite the importance of land surfaces as the lower boundary condition of atmospheric dynamics, few studies of the North American monsoon have directly quantified the diurnal cycle of surface energy fluxes or their link to precipitation [c.f., *Gutzler et al*., 2009]. The large degree of spatial heterogeneity of land surface conditions in the southwest U.S. and northwest Mexico presents a challenge for the observation and modeling of surface energy fluxes [*Bohn and Vivoni*, 2016]. As a result, identifying the dynamic nature of the coupling between the diurnal cycles of turbulent fluxes and the diurnal variations in precipitation has yet to be addressed using a coupled land-atmosphere modeling system. In this study, we take an important step toward addressing this question by evaluating the performance of the WRF-Hydro modeling system with the Noah-MP LSM in its ability to simulate the diurnal cycle of turbulent fluxes in regions of complex terrain with seasonally varying vegetation. Model evaluation activities are conducted for one-dimensional and distributed simulations in reference to multiple ground-based and remotely sensed observations as well as a set of coarser resolution land surface models from NLDAS. After assessing 1-D model performance against observations, we present a series of analyses of remotely sensed observations and a spatially distributed implementation of WRF-Hydro that are intended to identify the spatial and temporal variabilities of the diurnal cycle of surface energy fluxes and their potential link to precipitation patterns. Results from the study reveal the following main conclusions:

1. Using calibrated soil hydraulic parameters, WRF-Hydro is able to reproduce the observed soil moisture and turbulent fluxes during calibration and validation periods as evaluated at individual sites. Discrepancies between the 1-D and distributed simulations were primarily attributed to the differences in precipitation forcing between local rain gauges and bias-corrected NLDAS fields. Comparisons of the spatial patterns produced by WRF-Hydro with remotely sensed observations of ET, LST, and SM show reasonable model performance in the ability to simulate the diurnal cycle of land surface states and fluxes during the North American monsoon.
2. Based on this model performance, the simulated diurnal cycle of turbulent fluxes is found to vary in space and time as a function of the seasonal evolution of the NAM, ecosystem type, and presence of soil water indicated through a classification into rainy and nonrainy days. The diurnal cycle of latent heat flux is more sensitive than sensible heat flux in its spatiotemporal variability, exhibiting clear patterns across the major ecosystems and for different wetness states. The sensitivity of the diurnal cycle of latent heat flux is associated primarily to the variations of plant transpiration in response to soil water content through its control on stomatal resistance.
3. The diurnal cycle of precipitation has an imprint on the diurnal cycle of latent heat flux through the sensitivity of plant transpiration. For rainy days in water-stressed ecosystems, the peak timing of precipitation affects the shape and magnitude of the diurnal cycle of plant transpiration, typically leading to a more robust ET response that is sustained for longer periods of the day. This delay in the diurnal peak of

plant transpiration is attributed to a release of midday stomatal closure that is typically required in water-stressed ecosystems and ultimately implies an accelerated return of soil water back to the atmosphere as evapotranspiration.

4. Within the distributed simulations, plant transpiration is responsible for large spatial contrasts in the diurnal cycle of the turbulent fluxes, which induce mesoscale heterogeneity in land surface conditions. WRF-Hydro demonstrates reasonable fidelity in depicting landscape-scale variations in surface energy fluxes that are generated by spatial variability of terrain, soil, and vegetation conditions. Spatiotemporal comparisons to the diurnal cycle simulated by three NLDAS LSMs indicate that this spatial feature as well as the overall shapes and magnitudes for specific ecosystems are not reproduced well in the coarser resolution models, indicating potential limitations in their representation of mesoscale circulations and convective precipitation.

While our comparisons show that the distributed WRF-Hydro simulations could reasonably reproduce many of the observed spatial patterns obtained from remote-sensing products, we could not clearly isolate which of the different process representations (e.g., vegetation dynamics, differing plant transpiration functions, differing soil class calibrations, or the impact of plant rooting depth) contributed the most sensitivity to the patterns produced by the modeling system. We identified through comparisons of distributed WRF-Hydro (with routing on or off) and 1-D Noah-MP that topographic redistribution affects the spatial patterns of soil water content and energy partitioning, in particular for riparian zones, but the impacts are smaller than anticipated in more humid areas, consistent with the observations of *Vivoni et al.* [2007] across an elevation transect. In order to diagnose the role of individual vegetation processes or parameters contributing to the simulated patterns, additional sensitivity experiments would be fruitful. Such a process-level diagnosis of the approach also requires further coordinated observational-modeling investigations in the region, possibly through an intercomparison between spatially distributed modeling systems [e.g., *Kollet and Maxwell*, 2008; *Mascaro et al*., 2015].

To our knowledge, this is the first study to characterize the spatiotemporal variability of the diurnal cycle of surface energy fluxes and its relation with the diurnal cycle of precipitation during the North American monsoon. This work was made possible by advances in the high-resolution simulation of regional land surface processes in the WRF-Hydro modeling system and other land surface models that can account for topographic variability and seasonal vegetation dynamics. Furthermore, WRF-Hydro provides the ability to conduct regional to continental scale studies efficiently and opens the avenue for coupled (online) simulations that can represent the two-way feedback between the land surface and the atmosphere [e.g., *Senatore et al*., 2015]. In addition, the biophysical processes represented in Noah-MP, for example, the effect of soil water on the diurnal cycle of plant transpiration through stomatal closure, provide a means to bridge the gap between local ecosystem processes and interactions between vegetation, terrain, and atmospheric conditions at the regional scale. As a result, it is possible to study the impacts of the mesoscale organization and heterogeneity of surface turbulent fluxes on atmospheric boundary layer dynamics. Fruitful avenues of study include determining if these new representations of diurnal cycle of turbulent fluxes can further alter background atmospheric circulations such as mountain-valley circulations and convective precipitation through the use of coupled simulations.

Acknowledgments
We acknowledge the funding support from the NOAA Climate Program Office (grant NA10OAR4310165), NASA Headquarters under the Earth and Space Science Fellowship program (grant NNX15AP05H), and National Science Foundation International Research Experience for Students program (grants OISE 0553852 and OISE 0809946). E.R.V. would like to thank the U.S. Fulbright-Garcia Robles and Mexican CONACYT fellowships for support. We would like to thank Agustin Robles-Morua, Julio C. Rodríguez, Christopher J. Watts, and Jaime Garatuza-Payán for their help in field data collection and processing. Field data products can be obtained from https://hrsl.ba.ars.usda.gov/smex04/ and http://vivoni.asu.edu/sonora/www/, while model outputs and forcings from the North American Land Data Assimilation System are available at https://ldas.gsfc.nasa.gov/nldas/NLDAS2forcing.php. We also acknowledge support from Michael Barlage, Aubrey Dugger, and the rest of the WRF-Hydro development team at the National Center for Atmospheric Research. WRF-Hydro is available for download from https://ral.ucar.edu/projects/wrf_hydro. Finally, we thank the excellent comments from anonymous reviewers and the editors of the journal that helped to improve the manuscript.

References

Adams, D. K., and A. C. Comrie (1997), The North American monsoon, *Bull. Am. Meteorol. Soc.*, *78*, 2197–2213.

Ball, J. T., I. E. Woodrow, and J. A. Berry (1987), A model predicting stomatal conductance and its contribution to the control of photosynthesis under different environmental conditions, in *Process in Photosynthesis Research*, vol. 1, edited by J. Biggins, pp. 221–234, Martinus Nijhoff, Dordrecht, Netherlands.

Betts, A. K., J. H. Ball, A. C. M. Beljaars, M. J. Miller, and P. A. Viterbo (1996), The land surface-atmosphere interaction: A review based on observational and global modeling perspectives, *J. Geophys. Res.*, *101*(D3), 7209–7225, doi:10.1029/95JD02135.

Beven, K., R. Lamb, P. Quinn, R. Romanowicz, J. Freer, and V. Singh (1995), Topmodel, in *Computer Models of Watershed Hydrology*, edited by V. P. Singh, pp. 627–668, Water Resour. Publ., Ann Arbor, Mich.

Bohn, T. J., and E. R. Vivoni (2016), Process-based characterization of evapotranspiration sources over the North American monsoon region, *Water Resour. Res.*, *52*, 358–384, doi:10.1002/2015WR017934.

Boone, A., et al. (2004), The Rhône-Aggregation Land Surface Scheme Intercomparison Project: An overview, *J. Clim.*, *17*, 187–208.

Boone, A., et al. (2009), The AMMA land surface model intercomparison project, *Bull. Am. Meteorol. Soc.*, *90*, 1865–1880.

Brutsaert, W. A. (1982), *Evaporation into the Atmosphere*, 299 pp., D. Reidel, Dordrecht, Netherlands.

Castro, C., H. Chang, F. Dominguez, C. Carrillo, J. Schemm, and J. H. Henry (2012), Can a regional climate model improve the ability to forecast the North American monsoon?, *J. Clim.*, *25*, 8212–8237.

Chen, F., K. Mitchell, J. Schaake, Y. Xue, H. Pan, V. Koren, Y. Duan, M. Ek, and A. Betts (1996), Modeling of land-surface evaporation by four schemes and comparison with FIFE observations, *J. Geophys. Res.*, *101*, 7251–7268, doi:10.1029/95JD02165.

Choi, H. I., X. Z. Liang, and P. Kumar (2013), A conjunctive surface-subsurface flow representation for mesoscale land surface models, *J. Hydrometeorol.*, *14*(5), 1421–1442.

Collier, J. C., and G. J. Zhang (2006), Simulation of the North American monsoon by the NCAR CCM3 and its sensitivity to convection parameterization, *J. Clim.*, *19*, 2851–2866.

Collins, D. B. G., and R. L. Bras (2007), Plant rooting strategies in water-limited ecosystems, *Water Resour. Res.*, *43*, W06407, doi:10.1029/2006WR005541.

Dirmeyer, P. A., A. J. Dolman, and N. Sato (1999), The Global Soil Wetness Project: A pilot project for global land surface modeling and validation, *Bull. Am. Meteorol. Soc.*, *80*, 851–878.

Dominguez, F., P. Kumar, and E. R. Vivoni (2008), Precipitation recycling variability and ecoclimatological stability—A study using NARR data. Part II: North American monsoon region, *J. Clim.*, *21*(20), 5187–5203.

Douglas, M. W., R. A. Maddox, K. Howard, and S. Reyes (1993), The Mexican monsoon, *J. Clim.*, *6*, 1665–1677.

Eltahir, E. A. B. (1998), A soil moisture-rainfall feedback mechanism: 1. Theory and observations, *Water Resour. Res.*, *34*, 765–776, doi:10.1029/97WR03499.

Ek, M. B., K. E. Mitchell, Y. Lin, E. Rogers, P. Grunmann, V. Koren, G. Gayno, and J. D. Tarpley (2003), Implementation of Noah land surface model advances in the National Centers for environmental prediction operational mesoscale eta model, *J. Geophys. Res.*, *108*(D22), 8851, doi:10.1029/2002JD003296.

Feng, X., M. Bosilovich, P. Houser, and J.-D. Chern (2013), Impact of land surface conditions on 2004 North American monsoon in GCM experiments, *J. Geophys. Res. Atmos.*, *118*, 293–305, doi:10.1029/2012JD018805.

Fensholt, R., I. Sanholt, and M. Schultz (2004), Evaluation of MODIS LAI, fAPAR and the relation between fAPAR and NDVI in a semiarid environment using in situ measurements, *Remote Sens. Environ.*, *91*, 490–507.

Forzieri, G., F. Castelli, and E. R. Vivoni (2011), Vegetation dynamics within the North American monsoon region, *J. Clim.*, *24*, 1763–1783.

Forzieri, G., L. Feyen, A. Cescatti, and E. R. Vivoni (2014), Spatial and temporal variations in ecosystem response to monsoon precipitation variability in southwestern North America, *J. Geophys. Res. Atmos.*, *119*, 1999–2017, doi:10.1002/2014JG002710.

Gao, X., J. Li, and S. Sorooshian (2007), Modeling intraseasonal features of 2004 North American monsoon precipitation, *J. Clim.*, *20*, 1882–1896.

Gebremichael, M., E. R. Vivoni, C. J. Watts, and J. C. Rodriguez (2007), Submesoscale spatiotemporal variability of North American monsoon rainfall over complex terrain, *J. Clim.*, *20*, 1751–1773.

Glenn, E. P., R. L. Scott, U. Nguyen, and P. L. Nagler (2015), Wide-area ratios of evapotranspiration to precipitation in monsoon-dependent semiarid vegetation communities, *J. Arid Environ.*, *117*, 84–95.

Gochis, D. J., and F. Chen (2003), Hydrological enhancements to the community Noah land surface model: Technical description, NCAR Tech. Note, TN-454+STR, 77 pp., Boulder, Colo., doi:10.5065/D60P0X00.

Gochis, D. J., W. J. Shuttleworth, and Z. Yang (2002), Sensitivity of the modeled North American monsoon regional climate to convective parameterization, *Mon. Weather Rev.*, *130*, 1282–1298.

Gochis, D. J., C. J. Watts, J. Garatuza-Payán, and J. C. Rodriguez (2007), Spatial and temporal patterns of precipitation intensity as observed by the NAME event rain gauge network from 2002 to 2004, *J. Clim.*, *20*, 1734–1750.

Gochis, D. J., W. Yu, and D. N. Yates (2014), The WRF-Hydro model technical description and user's guide, version 2.0, NCAR Tech. Document, 120 pp., Boulder, Colo.

Goldstein, A. H., N. E. Hultman, J. M. Fracheboud, M. R. Bauer, J. A. Panek, M. Xu, Y. Qi, A. B. Guenther, and W. Baugh (2000), Effects of climate variability on the carbon dioxide, water, and sensible heat fluxes above a ponderosa pine plantation in the Sierra Nevada (CA), *Agric. For. Meteorol.*, *101*, 113–129.

Gutzler, D. S., et al. (2005), The North American Monsoon Model Assessment Project: Integrating numerical modeling into a field-based process study, *Bull. Am. Meteorol. Soc.*, *86*, 1423–1429.

Gutzler, D. S., et al. (2009), Simulations of the 2004 North American monsoon: NAMAP2, *J. Clim.*, *22*, 6716–6740.

Hallack-Alegría, M., and D. W. Watkins (2007), Annual and warm season drought intensity-duration-frequency analysis for Sonora, Mexico, *J. Clim.*, *20*, 1897–1909.

Higgins, W., and D. J. Gochis (2007), Synthesis of results from the North American Monsoon Experiment (NAME) process study, *J. Clim.*, *20*, 1601–1607.

Instituto Nacional de Estadística, Geografía e Informática (INEGI) (2007), Conjunto de Datos Vectorial Edafológico, 1:250,000, Serie II (Continuo Nacional), Mexico.

Ivanov, V. Y., E. R. Vivoni, R. L. Bras, and D. Entekhabi (2004), Catchment hydrologic response with a fully-distributed triangulated irregular network model, *Water Resour. Res.*, *40*, W11102, doi:10.1029/2004WR003218.

Jordan, R. (1991), *A One-Dimensional Temperature Model for a Snow Cover*, *Spec. Rep*, vol. 91–16, Cold Reg. Res. and Eng. Lab., U.S. Army Corps of Eng, Hanover, N. H.

Jovanovic, N., M. Masiyandima, V. Naiken, S. Dzikiti, and M. Gush (2012), Remote sensing applications in water resources management—Desktop validation and draft paper; CSIR Rep. No. CSIR/NRE/ECOS/IR/2011/0097/A; CSIR: Pretoria, South Africa.

Kollet, S. J., and R. M. Maxwell (2008), Capturing the influence of groundwater dynamics on land surface processes using an integrated, distributed watershed model, *Water Resour. Res.*, *44*, W02402, doi:10.1029/2007WR006004.

Koster, R. D., and M. J. Suarez (1992), Modeling the land surface boundary in climate models as a composite of independent vegetation stands, *J. Geophys. Res.*, *97*(D3), 2697–2715, doi:10.1029/91JD01696.

Koster, R. D., and M. J. Suarez (1994), The components of a SVAT scheme and their effects on a GCM's hydrological cycle, *Adv. Water Resour.*, *17*, 61–78.

Kumar, A., F. Chen, M. J. Barlage, M. B. Ek, and D. Niyogi (2014), Assessing impacts of integrating MODIS vegetation data in the Weather Research and Forecasting model coupled to two different canopy-resistance approaches, *J. Appl. Meteorol. Climatol.*, *53*, 1362–1380.

Lee, M.-I., S. D. Schubert, M. J. Suarez, I. M. Held, N.-C. Lau, J. J. Ploshay, A. Kumar, H.-K. Kim, and J.-K. E. Schemm (2007), An analysis of the warm season diurnal cycle over the continental United States and northern Mexico in general circulation models, *J. Hydrometeorol.*, *8*, 344–366.

Lee, M.-I., S. Schubert, M. Suarez, J. Schemm, H. Pan, J. Han, and S. Yoo (2008), Role of convection triggers in the simulation of the diurnal cycle of precipitation over the United States Great Plains in a general circulation model, *J. Geophys. Res.*, *113*, D02111, doi:10.1029/2007JD008984.

Lehner, B., K. Verdin, and A. Jarvis (2008), New global hydrography derived from spaceborne elevation data, *Eos Trans. AGU*, *89*, 93–94.

Lehning, M., I. Völksch, D. Gustafsson, T. A. Nguyen, M. Stähli, and M. Zappa (2006), ALPINE3D: A detailed model of mountain surface processes and its application to snow hydrology, *Hydrol. Processes*, *20*(10), 2111–2128.
Li, J., X. Gao, R. A. Maddox, and S. Sorooshian (2004), Model study of evolution and diurnal variations of rainfall in the North American monsoon during June and July 2002, *Mon. Weather Rev.*, *132*, 2895–2915.
Liang, X., D. P. Lettenmaier, E. F. Wood, and S. J. Burges (1994), A simple hydrologically based model of land surface water and energy fluxes for general circulation models, *J. Geophys. Res.*, *99*, 14,415–14,428, doi:10.1029/94JD00483.
Liang, X., X. Liang, J. Zhu, K. Kunkel, and M. Ting (2008), Do CGCMs simulate the North American monsoon precipitation seasonal-interannual variability?, *J. Clim.*, *21*, 4424–4448.
Livneh, B., E. A. Rosenberg, C. Y. Lin, B. Nijssen, V. Mishra, K. M. Andreadis, E. P. Maurer, and D. P. Lettenmaier (2013), A long-term hydrologically based dataset of land surface fluxes and states for the conterminous United States: Update and extensions, *J. Clim.*, *26*(23), 9384–9392.
Loveland, T. R., B. C. Reed, J. F. Brown, D. O. Ohlen, Z. Zhu, L. Yang, and J. W. Merchant (2000), Development of a global land cover characteristics database and IGBP DISCover from 1 km AVHRR data, *Int. J. Remote Sens.*, *21*, 1303–1330.
Mahrt, L., and H.-L. Pan (1984), A two-layer model of soil hydrology, *Boundary Layer Meteorol.*, *29*, 1–20.
Manabe, S. (1969), Climate and the ocean circulation: 1, the atmospheric circulation and the hydrology of the Earth's surface, *Mon. Weather Rev.*, *97*, 739–805.
Mascaro, G., and E. R. Vivoni (2012), Utility of coarse and downscaled soil moisture products at L-band for hydrologic modeling at the catchment scale, *Geophys. Res. Lett.*, *39*, L10403, doi:10.1029/2012GL051809.
Mascaro, G., E. R. Vivoni, D. J. Gochis, C. J. Watts, and J. C. Rodríguez (2014), Temporal downscaling and statistical analysis of rainfall across a topographic transect in northwest Mexico, *J. Appl. Meteorol. Climatol.*, *53*, 910–927.
Mascaro, G., E. R. Vivoni, and L. A. Méndez-Barroso (2015), Hyperresolution hydrologic modeling in a regional watershed and its interpretation using empirical orthogonal functions, *Adv. Water Resour.*, *83*, 190–206.
Méndez-Barroso, L. A., and E. R. Vivoni (2010), Observed shifts in land surface conditions during the North American monsoon: Implications for a vegetation-rainfall feedback mechanism, *J. Arid Environ.*, *74*, 549–555.
Méndez-Barroso, L. A., E. R. Vivoni, A. Robles-Morua, G. Mascaro, E. A. Yépez, J. C. Rodríguez, C. J. Watts, J. Garatuza-Payán, and J. Saíz-Hernandez (2014), A modeling approach reveals differences in evapotranspiration and its partitioning in two semiarid ecosystems in northwest Mexico, *Water Resour. Res.*, *50*, 3229–3252, doi:10.1002/2013WR014838.
Mitchell, K. E., et al. (2004), The multi-institution North American Land Data Assimilation System (NLDAS): Utilizing multiple GCIP products and partners in a continental distributed hydrological modeling system, *J. Geophys. Res.*, *109*, D07S90, doi:10.1029/2003JD003823.
Mo, K. C., L. N. Long, Y. Xia, S. K. Yang, J. E. Schemm, and M. Ek (2011), Drought indices based on the climate forecast system reanalysis and ensemble NLDAS, *J. Hydrometeorol.*, *12*, 181–205.
Mu, Q., M. Zhao, and S. W. Running (2011), Improvements to a MODIS global terrestrial evapotranspiration algorithm, *Remote Sens. Environ.*, *115*, 1781–1800.
Nesbitt, S. W., D. J. Gochis, and T. J. Lang (2008), The diurnal cycle of clouds and precipitation along the Sierra Madre Occidental observed during NAME-2004: Implications for warm season precipitation estimation in complex terrain, *J. Hydrometeorol.*, *9*, 728–743.
Niu, G.-Y., and Z.-L. Yang (2004), The effects of canopy processes on snow surface energy and mass balances, *J. Geophys. Res.*, *109*, D23111, doi:10.1029/2004JD004884.
Niu, G.-Y., and Z.-L. Yang (2006), Effects of frozen soil on snowmelt runoff and soil water storage at a continental scale, *J. Hydrometeorol.*, *7*, 937–952.
Niu, G.-Y., et al. (2011), The community Noah land surface model with multiparameterization options (Noah-MP): 1. Model description and evaluation with local-scale measurements, *J. Geophys. Res.*, *116*, D12109, doi:10.1029/2010JD015139.
Ogle, K., and J. F. Reynolds (2004), Plant responses to precipitation in desert ecosystems: Integrating functional types, pulses, thresholds, and delays, *Oecologia*, *141*, 282–294.
Pan, H.-L., and L. Mahrt (1987), Interaction between soil hydrology and boundary layer development, *Boundary Layer Meteorol.*, *38*, 185–202.
Pan, M., et al. (2003), Snow process modeling in the North American Land Data Assimilation System (NLDAS): 2. Evaluation of model simulated snow water equivalent, *J. Geophys. Res.*, *108*(D22), 8850, doi:10.1029/2003JD003994.
Pérez-Ruíz, E. R., J. Garatuza-Payán, C. J. Watts, J. C. Rodríguez, E. A. Yépez, and R. L. Scott (2010), Carbon dioxide and water vapour exchange in a tropical dry forest as influenced by the North American Monsoon System (NAMS), *J. Arid Environ.*, *74*, 556–563.
Pierini, N. A., E. R. Vivoni, A. Robles-Morua, R. L. Scott, and M. A. Nearing (2014), Using observations and a distributed hydrologic model to explore runoff threshold processes linked with mesquite encroachment in the Sonoran Desert, *Water Resour. Res.*, *50*, 8191–8215, doi:10.1002/2014WR015781.
Pitman, A. J. (2003), The evolution of, and revolution in, land surface schemes designed for climate models, *Int. J. Climatol.*, *23*, 479–510.
Privette, J. L., R. B. Myneni, Y. Knyazikhin, M. Mukelabai, and G. Roberts (2002), Early spatial and temporal validation of MODIS LAI product in the Southern Africa Kalahari, *Remote Sens. Environ.*, *83*, 232–243.
Ramoelo, A., N. Majozi, R. Mathieu, N. Jovanovic, A. Nickless, and S. Dzikiti (2014), Validation of global evapotranspiration product (MOD16) using flux tower data in the African savanna, South Africa, *Remote Sens.*, *6*, 7406–7423.
Robles-Morua, A., E. R. Vivoni, and A. S. Mayer (2012), Distributed hydrologic modeling in northwest Mexico reveals the links between runoff mechanisms and evapotranspiration, *J. Hydrometeorol.*, *13*, 785–807.
Robles-Morua, A., D. Che, A. S. Mayer, and E. R. Vivoni (2015), Hydrologic assessment of proposed reservoirs in the Sonora River Basin, Mexico, under historical and future climate scenarios, *Hydrol. Sci. J.*, *60*, 50–66.
Rosero, E., Z.-L. Yang, T. Wagener, L. E. Gulden, S. Yatheendradas, and G.-Y. Niu (2010), Quantifying parameter sensitivity, interaction, and transferability in hydrologically enhanced versions of the Noah land surface model over transition zones during the warm season, *J. Geophys. Res.*, *115*, D03106, doi:10.1029/2009JD012035.
Ryu, D., T. J. Jackson, R. Bindlish, D. M. Le Vine, and M. Haken (2010), Soil moisture retrieval using a two-dimensional L-band synthetic aperture radiometer in a semiarid environment, *IEEE Trans. Geosci. Remote Sens.*, *48*, 4273–4284.
Ryu, Y., J. Verfaille, C. Macfarlane, H. Kobayashi, O. Sonnentag, R. Vargas, S. Ma, and D. Baldocchi (2012), Continuous observations of tree leaf area index at ecosystem scale using upward-pointing digital cameras, *Remote Sens. Environ.*, *126*, 115–125.
Seastrand, S., Y. Serra, C. Castro, and E. Ritchie (2015), The dominant synoptic-scale modes of North American monsoon precipitation, *Int. J. Climatol.*, *35*, 2019–2032.
Sellers, P. J., et al. (1997), Modelling the exchanges of energy, water and carbon between continents and the atmosphere, *Science*, *275*, 502–509.

Senatore, A., G. Mendicino, D. J. Gochis, W. Yu, D. N. Yates, and H. Kunstmann (2015), Fully coupled atmosphere-hydrology simulations for the central Mediterranean: Impact of enhanced hydrological parameterization for short and long time scales, *J. Adv. Model. Earth Syst.*, *7*, 1693–1715, doi:10.1002/2015MS000510.

Schaake, J. C., V. I. Koren, Q.-Y. Duan, K. E. Mitchell, and F. Chen (1996), Simple water balance model for estimating runoff at different spatial and temporal scales, *J. Geophys. Res.*, *101*, 7461–7475, doi:10.1029/95JD02892.

Schiffer, N. J., and S. W. Nesbitt (2012), Flow, moisture, and thermodynamic variability associated with Gulf of California surges in the North American monsoon, *J. Clim.*, *25*, 4220–4241.

Stensrud, D. J. (2013), Upscale effects of deep convection during the North American monsoon, *J. Atmos. Sci.*, *70*, 2681–2695.

Sturman, A. P., H. A. McGowan, and R. A. Spronken-Smith (1999), Mesoscale and local climates, *Prog. Phys. Geogr.*, *23*, 611–635.

Vivoni, E. R. (2012), Diagnosing seasonal vegetation impacts on evapotranspiration and its partitioning at the catchment scale during SMEX04-NAME, *J. Hydrometeorol.*, *13*, 1631–1638.

Vivoni, E. R., et al. (2007), Variation of hydrometeorological conditions along a topographic transect in northwestern Mexico during the North American monsoon, *J. Clim.*, *20*, 1792–1809.

Vivoni, E. R., M. Gebremichael, C. J. Watts, R. Bindlish, and T. J. Jackson (2008a), Comparison of ground-based and remotely-sensed surface soil moisture estimates over complex terrain during SMEX04, *Remote Sens. Environ.*, *112*, 314–325.

Vivoni, E. R., H. A. Moreno, G. Mascaro, J. C. Rodríguez, C. J. Watts, J. Garatuza-Payán, and R. L. Scott (2008b), Observed relation between evapotranspiration and soil moisture in the North American monsoon region, *Geophys. Res. Lett.*, *35*, L22403, doi:10.1029/2008GL036001.

Vivoni, E. R., J. C. Rodríguez, and C. J. Watts (2010), On the spatiotemporal variability of soil moisture and evapotranspiration in a mountainous basin within the North American monsoon region, *Water Resour. Res.*, *46*, W02509, doi:10.1029/2009WR008240.

Wan, Z., and J. Dozier (1996), A generalized split-window algorithm for retrieving land surface temperature from space, *IEEE Trans. Geosci. Remote Sens.*, *34*, 892–905.

Whiteman, C. D., S. Zhong, X. Bian, J. D. Fast, and J. C. Doran (2000), Boundary layer evolution and regional-scale diurnal circulations over the Mexico Basin and Mexican Plateau, *J. Geophys. Res.*, *105*, 10,081–10,102, doi:10.1029/2000JD900039.

Wigmosta, M. S., L. W. Vail, and D. P. Lettenmaier (1994), A distributed hydrology-vegetation model for complex terrain, *Water Resour. Res.*, *30*(6), 1665–1680, doi:10.1029/94WR00436.

Wilson, K. B., D. Baldocchi, and E. Fadge (2003), Diurnal centroid of ecosystem energy and carbon fluxes at FLUXNET sites, *J. Geophys. Res.*, *108*(D21), 4664, doi:10.1029/2001JD001349.

Wood, E. F., D. Lettenmaier, X. Liang, B. Nijssen, and S. W. Wetzel (1997), Hydrological modeling of continental-scale basins, *Annu. Rev. Earth Planet. Sci.*, *25*, 279–300.

Xia, Y., et al. (2012), Continental-scale water and energy flux analysis and validation for the North-American Land Data Assimilation System Project phase 2 (NLDAS-2). Part 1: Comparison analysis and application of model products, *J. Geophys. Res.*, *117*, D03109, doi:10.1029/2011JD016048.

Xia, Y., M. T. Hobbins, Q. Mu, and M. B. Ek (2015), Evaluation of NLDAS-2 evapotranspiration against tower flux site observations, *Hydrol. Processes*, *29*, 1757–1771.

Xiang, T., E. R. Vivoni, and D. J. Gochis (2014), Seasonal evolution of ecohydrological controls on land surface temperature over complex terrain, *Water Resour. Res.*, *50*, 3852–3874, doi:10.1002/2013WR014787.

Yamada, T. J., M.-I. Lee, M. Kanamitsu, and H. Kanamaru (2012), Diurnal characteristics of rainfall over the contiguous United States and northern Mexico in the dynamically downscaled reanalysis dataset (US10), *J. Hydrometeorol.*, *13*, 1142–1148.

Yang, Z.-L., R. E. Dickinson, A. Robock, and K. Y. Vinnikov (1997), Validation of the snow sub-model of the biosphere-atmosphere transfer scheme with Russian snow cover and meteorological observational data, *J. Clim.*, *10*, 353–373.

Yucel, I., A. Onen, K. K. Yilmaz, and D. J. Gochis (2015), Calibration and evaluation of a flood forecasting system: Utility of numerical weather prediction model, data assimilation and satellite-based rainfall, *J. Hydrol.*, *523*, 49–66.